Permeation and Stability Properties of Asymmetric and Disk Shaped Oxygen Permeable Membranes Intended for Syn-Gas Production

Nils Wagner

" Wenn ich Schriften trauen kann, warum trauern wir dann?"

Michael Galla † 9. August 2011 Bochum Germany

"Finally the tables are starting to turn Talking about a revolution"

Tracy Chapman

Declaration

This project has been carried out at:

Norwegian University of Science and Technology (NTNU)

Department of Material Science and Engineering

Sem Sælandsvei 12 N-7034 Trondheim Norway

Supervisors:

Professor Dr. Thomas Jüstel   Münster University of Applied Sciences

Professor Dr. Kjell Wiik   NTNU Trondheim

Co Supervisors:

Dr. Jonas Gurauskis   NTNU Trondheim

Ph.D. Candidate Ørjan Fossmark Lohne   NTNU Trondheim

M.Sc. Candidate:

Nils Wagner

Hemberger Damm 23 48282 Emsdetten Germany

Fachhochschule Münster

Department: Chemical engineering

Matriculation number: 568633

The thesis was delivered to the Audit Committee of the chemical engineering department

on the _____

I hereby affirm that the work in this study has been conducted honestly, independently
and all used references are denoted.

Place/Date   Sign

Abstract

In this study, the oxygen permeation and stability properties of disk shaped and asymmetric membranes, both of the composition $La_{0.2}Sr_{0.8}Fe_{0.8}Al_{0.2}O_{3-\delta}$ were investigated. Strontium doped Lanthanum ferrite is an oxygen deficient mixed ionic electronic conducting perovskite related material. Co-doping with Aluminum enhances the stability of the system.

Received precursor was ball milled and sieved to 250 μm. Phase purity was determined by means of X-ray diffraction. Further on particle size distribution and surface area data were collected by dynamic light scattering and nitrogen absorption (BET).

Ceramic disks were fabricated by dry uniaxial dye pressing and sintered at different temperatures. Densities of green bodies were measured by geometric means to be approximately 40% of theor. and final densities were measured using Archimedes method. to be approximately 96% of theor. at a sintering temperature of 1230 °C for 2 h in air.

Asymmetric membranes consist of a porous support and a dense functional layer. For preparation of porous supports the powder precursor was mixed with 30 wt-% carbon black and 3 wt-% ethyl cellulose. Supports were calcined at 950 °C and then dip coated with a stabilized suspension of $La_{0.2}Sr_{0.8}Fe_{0.8}Al_{0.2}O_{3-\delta}$ in ethanol. After dip coating, membranes were pre sintered at 1100 °C, dip coated again and finally sintered at different temperatures. Visual densities were investigated by scanning electron microscopy. Final sintering parameters were 1230 °C for 2 h respectively.

Furthermore, investigations on surface modification were carried out by wet chemical etching using 6M hydrochloric acid, resulting in a partly or complete dissolved functional layer.

Oxygen flux of membranes was finally measured in a flux furnace with coupled gas chromatograph.

Disk shaped membranes reached oxygen flux values up to 1.77 ml*min^{-1}*cm^{-2} and asymmetric membranes up to 15.33 ml*min^{-1}*cm^{-2}. After flux measurements were completed, the membranes were checked for degradation by means of XRD and SEM/EDS. Both, disk shaped and asymmetric membranes were overall single phase but showed some morphological degradation.

Table of contents

List of Figures

List of Tables

List of Acronyms

XRD	X-ray diffratometry
SEM	Scanning electron microscopy
EDS	Energy dispersive X-ray spectroscopy
TGA	Thermo gravimetric analysis
DLS	Dynamic light scattering
MIEC	Mixed ionic electronic conductor
LSFAl 2882	$La_{0.2}Sr_{0.8}Fe_{0.8}Al_{0.2}O_{3-\delta}$
LSF	$La_{1-x}Sr_xFeO_{3-\delta}$
LSFTa 2882	$La_{0.2}Sr_{0.8}Fe_{0.8}Ta_{0.2}O_{3-\delta}$
SE	Secondary electron detector
BSE	Back scatter electron detector

1 Introduction

Steadily increasing energy needs in nowadays society forces continuous research for alternative environmentally friendly energy production techniques. Since crude oil reserves will run short in the future, natural gas becomes a major important energy source. The reforming of natural gas to liquid fuels is mostly done by Fischer-Tropsch - and Methanol - synthesis.[1,2,4,19] Both require synthesis gas ($H_2 + CO$) as feedstock. Syn-gas was classically produced by means of methane steam reforming. This strongly endothermic reaction needs a huge amount of energy and ends in a syn-gas ratio of 3 (H_2) / 1 (CO) which is not adequate neither for F-T nor for methanol synthesis.[4]. Furthermore green house effect induced global warming demands environmentally friendly alternatives for syn-gas production, especially taking carbon capture and storage into account. A more modern approach for syn-gas production is the partially oxidation of methane. This process is slightly exothermic and results in a syn-gas ratio of 2 (H_2) to 1 (CO).[4] Both steam reforming and partial oxidation are illustrated in the following reaction schemes 1.1 and 1.2:

$$CH_4 + H_2O \rightarrow 3H_2 + CO \qquad \Delta H \ (25\ °C) = 206.16 \ kJ/mol \qquad (1.1)$$

$$CH_4 + 1/2O_2 \rightarrow 2H_2 + CO \qquad \Delta H \ (25\ °C) = -36 \ kJ/mol \qquad (1.2)$$
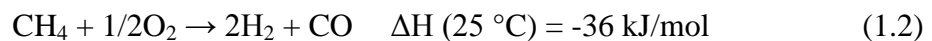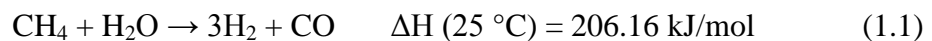
Since technological reasons require the absence of nitrogen in syn-gas mixtures huge amounts of pure oxygen are needed. Conventionally, pure oxygen is produced by means of cryogenic air distillation, which is an energy consuming process and thus makes the partially oxidation of methane very cost intensive if combined with cryogenic distillation.[4] An alternative is the partial oxidation of methane to syn-gas using mixed oxygen-ionic and electronic conducting membranes which are, in combination with a reforming catalyst, 100% selective for oxygen. This reduces syn-gas production to a single step process. Reliable catalysts which offer excellent methane oxidation levels and CO selectivity approaching 100% are e.g. Nickel or Rhodium.[1,4]

Mixed oxygen-ionic and electronic conducting materials (MIEC) offer the ability to separate oxygen from air electrochemically. Those materials are in scientific focus for important applications e.g. cathode materials for solid oxide fuel cells, oxygen sensors and oxygen permeable membranes.[1,2,19]

The driving force for oxygen ion diffusion in these materials is a difference in oxygen partial pressure and thus in chemical potential between both sides of a membrane. The operation principle of a mixed conducting membrane, including catalysts for syn-gas production, is illustrated in Fig. 1.1.
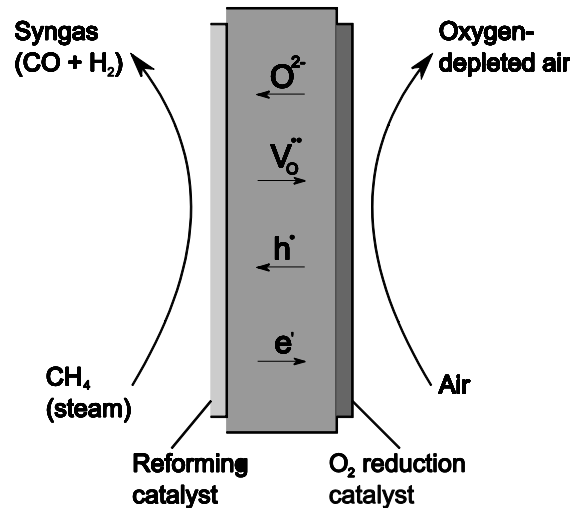
Figure 1.1: Schematic operation principle of a partially methane oxidation MIEC membrane reactor redrawn[1]

Several material systems are suitable for the operation principle. However since elevated operation temperature above 700 °C are normal, suitable membrane materials must offer high chemical and mechanical stabilities in oxidizing and severe reducing atmospheres even at these elevated temperatures. Furthermore, adequate oxygen flux which is either controlled by bulk diffusion or surface exchange respectively and low chemical and thermal expansion are required.[1,2] Promising materials, are acceptor doped, perovskite structured, Lanthanum cobaltites and ferrites. A-site doping is usually done by incorporation of Calcium, Strontium or Barium. Also mixtures and or complete substitution of Lanthanum can be found in literature. Mostly the B-site is doped as well to improve the system stability. This is mostly done by transition or main group metals.[1-4, 9-13, 27,29,30]

2 Objectives

This study is focused on the preparation, oxygen permeation and stability of mixed ionic electronic membranes intended for syn-gas production. Material composition used in this project is $La_{0.2}Sr_{0.8}Fe_{0.8}Al_{0.2}O_{3-\delta}$ later denoted as LSFAl 2882. The aim is to fabricate both disk shaped and asymmetric membranes, measure the oxygen permeation at normal and severe conditions at elevated temperatures, and investigate degradation of the samples after permeation measurements. Severe conditions are induced by exposing the sample to hydrogen containing atmosphere. Results will be discussed in relation to LSFTa 2882 membranes, produced and described by Gurauskis et al.[12,13,37]

3 Theory

3.1. Perovskites

The crystal structure of $CaTiO_3$ is referred to as perovskite structure. It consists of a large Ca^{2+} ion in the centre of the unit cell surrounded by corner shared $TiO_{6/2}$ octahedrons.[5] All AMX_3 compounds existing in this crystal structure are named perovskite related materials. A huge number of perovskite related compounds is feasible by variation of A- and M- cations due to structures tolerance of different bond length. Usually the X-atom is either oxygen or fluorine.[5] Basic combinations of oxide based perovskites are $A^{III}M^{III}O_3$, $A^{II}M^{IV}O_3$ and $A^{I}M^{V}O_3$.[6]

Ideal perovskite structure is cubic but can be distorted by a mismatch of the different equilibrium bond length which causes stresses in the perovskite structure. These stresses are reduced by cooperative rotations of $MX_{6/2}$ octahedrons. By this process the cubic ($Pm\overline{3}m$) space group symmetry is distorted. Normally rotations are about a cubic [001] axis which leads to tetragonal symmetries (I4 / mcm) and (P4 / mbm), a cubic [111] axis which leads to rhombohedral symmetries ($R\overline{3}c$) and ($Im\overline{3}$), or a cubic [110] axis ending in orthorhombic symmetries (Pbnm) and (Pnma). All changes in unit cell geometry also end in increased unit cell volume.[5] Fig. 3.1 shows the unit cell of $La_{0.2}Sr_{0.8}FeO_{3-\delta}$.
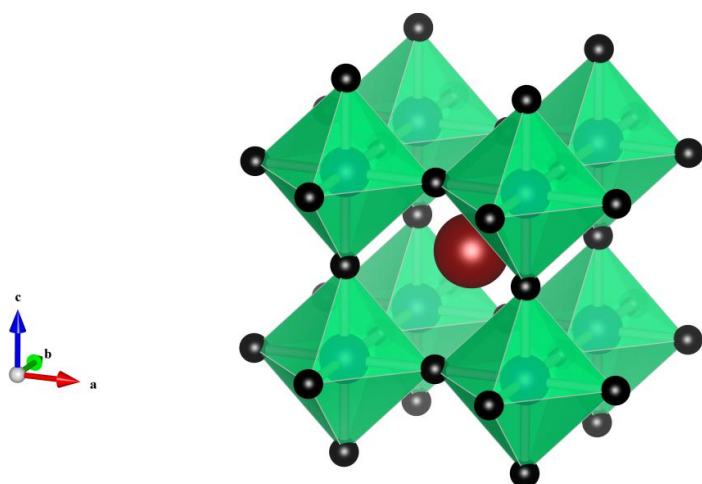
Figure 3.1: Visualization of a $La_{0.2}Sr_{0.8}FeO_{3-}\delta$ unit cell using Vesta and crystal data (1404417) of Pearson Crystal Database[31]

The symmetry of perovskite related materials can be predicted using Goldschmidt tolerance factor:[5-8]

$$t = \frac{r_A + r_o}{\sqrt{2}*(r_M + r_o)} \qquad (3.1.1)$$

Perovskite structure exists for tolerance factor $0.75 \leq t \leq 1.06$ where ideal cubic perovskites offer a tolerance factor of 1. Lower tolerance factors predict a distorted symmetry due to not ideal size ratio between A and M atoms.[7] The tolerance factor of LSFAl2882 was calculated to be 0.99 using ionic radii reported by R. D. Shannon, hence cubic symmetry can be predicted.[28]

The host lattice of LSFAl 2882 is Lanthanum ferrite ($LaFeO_3$) an orthorhombic perovskite offering a tolerance factor of 0.95. At ambient pressure and temperature $LaFeO_3$ is an antiferromagnetic insulator.[9,17] By doping $LaFeO_3$ with Sr^{2+} on the A-site symmetry transitions occur. Dependent on the Sr^{2+} content $La_{1-x}Sr_xFeO_{3-\delta}$ is orthorhombic for $0 \leq x \leq 0.2$, rhombohedral for $0.4 \leq x \leq 0.75$ or cubic for $0.75 \leq x \leq 1$. These transitions are temperature dependent, a pseudo-binary phase diagram for the system is given in Fig. 3.2. [10]
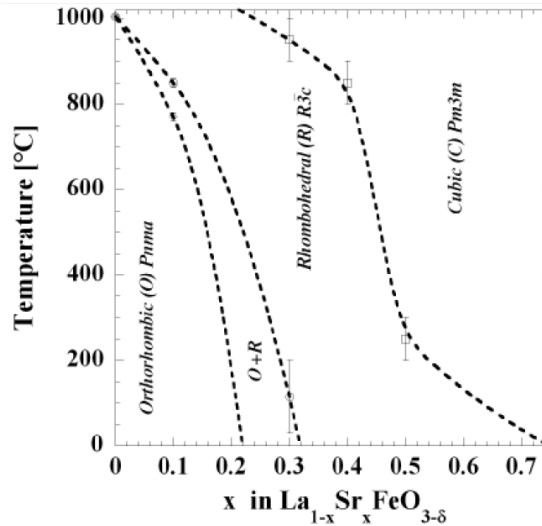
Figure 3.2: Pseudo-binary phase diagram of $La_{1-x}Sr_xFeO_{3-\delta}$[10]

The incorporation of 20 mol-% Al^{3+}, which offers a smaller ionic radius than $Fe^{3+/4+}$, on the B-site of $La_{0.2}Sr_{0.8}FeO_{3-\delta}$ raises the tolerance factor from 0.98 to 0.99. This value is close to unity (ideal perovskite).[11]

3.2 Defect chemistry

A large tolerance for oxygen vacancies is a major quality for the electrochemical properties of $La_{1-x}Sr_xFeO_{3-\delta}$.[6] Defect chemistry of this material can be described by a point defect model using Kröger-Vink notation.[6,14] Considered defects are Sr^{2+} on the A-site ($Sr_{La}^{/}$), Fe^{2+} and Fe^{4+} on the B-site ($Fe_{Fe}^{/}$ and $Fe_{Fe}^{\bullet}$) and oxygen vacancies ($V_o^{\bullet\bullet}$).[6]

Under oxidizing conditions $[Fe_{Fe}^{\bullet}] \gg [Fe_{Fe}^{/}]$, whereas at reducing conditions $[Fe_{Fe}^{/}] \gg [Fe_{Fe}^{\bullet}]$. Square brackets represent the concentration of each species in number of moles for one mole $La_{1-x}Sr_xFeO_{3-\delta}$ [15]. The presence of Fe^{4+} in Sr^{2+} doped Lanthanum ferrite was e.g. proven by S. E. Dann et al. using Mössbauer spectroscopy.[16]

The following equations describe the defect model of $La_{1-x}Sr_xFeO_{3-\delta}$ according to a model of Mizusaki et al. and I. Wærnhus.[6,15] Eq. 3.2.1 expresses the electro neutrality in the $La_{1-x}Sr_xFeO_{3-\delta}$ solid solution:

$$[Sr_{La}^{/}] + [Fe_{Fe}^{/}] = 2\,[V_o^{\bullet\bullet}] + [Fe_{Fe}^{\bullet}] \qquad (3.2.1)$$

$[Sr_{La}^{/}]$ is given by the A-site composition and can be described as x. Also the given system offers oxygen deficiency, hence $[V_o^{\bullet\bullet}]$ is described as δ. That leads to Eq. 3.2.2:

$$x + [Fe_{Fe}^{/}] = 2\,\delta + [Fe_{Fe}^{\bullet}] \qquad (3.2.2)$$

In oxidizing conditions Eq. (3.2.2) can be simplified to Eq. 3.2.2a:

$$x \approx 2\,\delta + [Fe_{Fe}^{\bullet}] \qquad (3.2.2a)$$

By decreasing the oxygen partial pressure (p_{O2}) the concentration of Fe^{4+} in the system becomes sufficiently low to allow the correlation:

$$x \approx 2\,\delta \qquad (3.2.2b)$$

Reducing conditions allow the simplification of Eq. 3.2.2 to:

$$x + [Fe'_{Fe}] \approx 2\,\delta \qquad\qquad (3.2.2c)$$

The defect concentrations as function of the logarithmic oxygen partial pressure (log p_{O2}) are given in the following diagram (Fig. 3.3). It is divided in III regions. Electro neutrality condition in region I can be described by Eq. 3.2.2a whereas Eq. 3.2.2c expresses conditions in region III. The plateau region (Region II) corresponds to Eq. 3.2.2b.
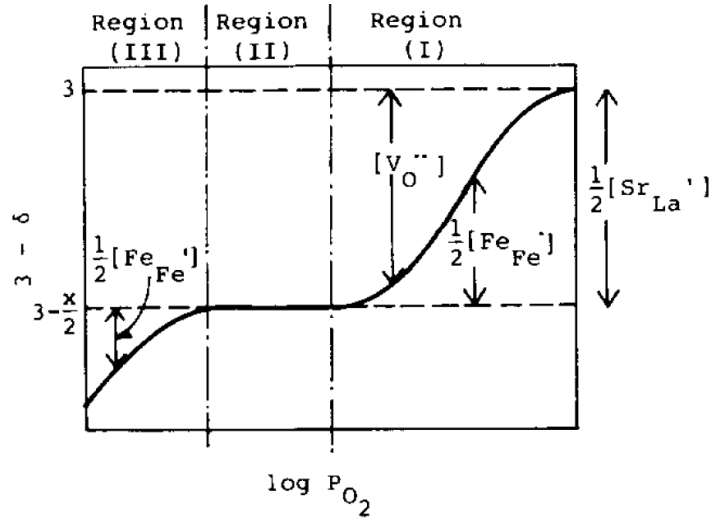
Figure 3.3: Schematic defect concentrations in La$_{1-x}$Sr$_x$FeO$_{3-\delta}$ as function of log p_{O2}.[15]

Interaction between gaseous oxygen and defects in the system is expressed by the following equilibrium:

$$\tfrac{1}{2}O_2(g) + V_o^{\bullet\bullet} + 2Fe_{Fe}^x \rightleftharpoons O_o^x + 2Fe_{Fe}^{\bullet} \qquad\qquad (3.2.3)$$
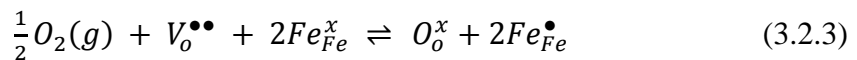
Assuming a random defect distribution and absence of interactive defects the equilibrium condition for this reaction is given by:

$$K_{ox} = \frac{[O_o^x] \times [Fe_{Fe}^{\bullet}]^2}{\sqrt{P_{O2}} \times [V_o^{\bullet\bullet}] \times [Fe_{Fe}^x]^2} \qquad\qquad (3.2.4)$$

Incorporation of oxygen into the corresponding vacancies leads to an increase in the iron valence due to charge compensation or in different expression due to oxygen reduction. Further the Fe^{3+} ions undergo disproportionation into Fe^{2+} and Fe^{4+}:

$$2Fe_{Fe}^x \rightleftharpoons Fe_{Fe}^{\bullet} + Fe_{Fe}^{/} \qquad (3.2.5)$$
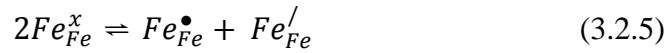
The disproportionation describes electron transfer between two Fe^{3+} ions. The equilibrium condition is given by:

$$K_i = \frac{[Fe_{Fe}^{\bullet}] \times [Fe_{Fe}^{/}]}{[Fe_{Fe}^x]^2} \qquad (3.2.6)$$

The substitution of La^{3+} by Sr^{2+} can be expresses by the following process:

$$SrFeO_3 \xrightarrow{LaFeO_3} Sr_{La}^{/} + Fe_{Fe}^{\bullet} + 3O_o^x \qquad (3.2.7)$$
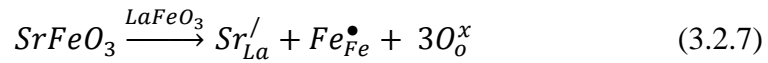
Since Sr^{2+} generates a negative charge on the A-site which is initially occupied by La^{3+} ions, Fe will be oxidized for charge compensation.

B-site substitution of Fe^{3+} by Al^{3+} does not create charge differences and can be basically described by:

$$LaAlO_3 \xrightarrow{LaFeO_3} La_{La}^x + Al_{Fe}^x + 3O_o^x \qquad (3.2.8)$$
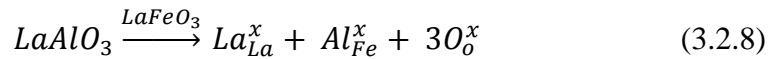
It is shown that B-site doping with Al^{3+} kinetically stabilizes the solid solution and inhibits the ordering of oxygen vacancies and thus the formation of a brownmillerite phase.[11] This structure ($A_2M_2O_5$) can be generated by removing one-sixth of the oxygen atoms of a cubic perovskite (AMO_3).[1]

3.3 Conductivity and oxygen diffusion

Sr^{2+} doped Lanthanum ferrite is a mixed conducting material. It offers electronic conductivity localized on the Fe-sites and ionic conductivity via oxygen vacancies.[6]
Electronic conductivity in Lanthanum ferrite materials is suggested to consist of small polaron hopping in the d-electron band formed by Fe ions. These are considered as localized electrons. The fraction of Fe^{2+} and Fe^{4+} gives the concentration of electrons and holes in the material as $n = [Fe^{2+}]$ and $p = [Fe^{4+}]$. Electronic conductivity is expressed by the following Eq.:[6,18]

$$\sigma_e = \frac{F}{V_m} \times [u_e \times n + u_h \times p]$$ (3.3.1)

Mobility of holes and electrons is represented by u_h and u_e, while n and p are the concentrations of Fe^{2+} and Fe^{4+}. The other symbols have their usual meaning.
The electronic conductivity is dependent on the population of Fe^{2+} and Fe^{4+} and thus strictly related to the oxygen non stoichiometry in the material.[6] Under the assumption that $u_h \approx u_e$ an average iron oxidation state of three causes a minimum conductivity value. Changing the oxidation state of iron by altering the oxygen partial pressure will generate either holes or electrons and hence contribute to a conductivity increase.[6]

In mixed ionic electronic conducting membranes a gradient in oxygen partial pressure (Δp_{O2}) is the driving force for oxygen permeation. Oxygen is transported from the side with a high oxygen partial pressure (p_{O2}) and thus a high chemical potential (μ_{O2}) to the side with a low p_{O2}.[1] A steady state profile of the chemical potential profile across a mixed ionic electronic conducting membrane is given in Fig.3.4.[1] To maintain electro neutrality in the system a continuous transport of electronic defects is required to gain a zero net transport.[2]
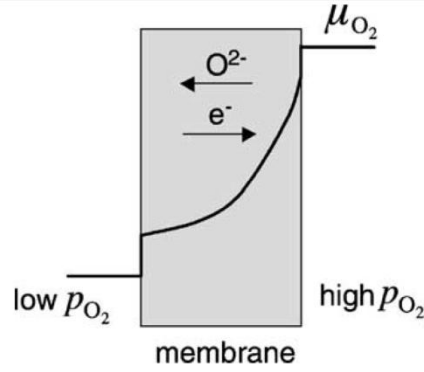
Figure 3.4: Oxygen chemical potential profile (μ_{O_2}) across a mixed ionic electronic conducting membrane at steady state condition.[1]

Since MIEC membranes are designed for operating under a chemical potential gradient, oxygen flux can be expressed by classical Wagner theory:[1,2]

$$J_{O2} = -\frac{1}{4^2 F^2} \times \frac{\sigma_{ion}\sigma_{el}}{\sigma_{ion}+\sigma_{el}} \times \nabla\mu_{O2} \qquad (3.3.2)$$

σ_{ion} and σ_{el} represent the partial conductivities of oxygen ionic and electronic defects. $\nabla\mu_{O2}$ is the oxygen chemical potential gradient. All other parameters have their usual meaning.

A substitution of the chemical potential with oxygen partial pressure (p_{O2}) and an integration over the membrane thickness L between the oxygen partial pressure on the air side (P_1) and on the fuel side (P_2) gives us the integrated Wagner Eq. for bulk diffusion:[2]

$$J_{O2} = \frac{RT}{4^2 F^2 L} \times \frac{\sigma_e \sigma_i}{\sigma_e+\sigma_i} (lnP_1 - lnP_2) \qquad (3.3.3)$$

This Eq. clarifies an increasing oxygen flux with decreasing membrane thickness for bulk controlled diffusion. If the membrane thickness is reduced to a critical value, the so called critical thickness L_c, oxygen transport is governed by surface exchange reactions and thus thickness independent. Literature values for the critical thickness of different LSF compositions are in the regime of 0.3-5500 µm. Critical thickness can be expressed by the chemical diffusion coefficient (D_{chem}) and the surface exchange coefficient (k_{chem}) as follows:[2,3,19]

$$L_c = \frac{D_{chem}}{k_{chem}} \tag{3.3.4}$$

Since asymmetric membranes manufactured in this study should offer thickness values $< L_c$ the surface exchange coefficient k_{chem} is the limiting factor for oxygen flux. Hence no further increase in the oxygen flux is feasible without increasing k_{chem}.

Oxygen transport in oxygen permeable MIEC membranes occurs exclusively via oxygen vacancies, hence a high $V_o^{\bullet\bullet}$ concentration is fundamental in order to achieve high oxygen fluxes.[2] It is not uncommon that acceptor doped perovskites exhibit 10-15% oxygen vacancies.[1] The proportionality of the oxygen vacancy concentration to the oxygen diffusion is given by the following Eq.:[2]

$$D_o = D_{V_o^{\bullet\bullet}} \times [V_o^{\bullet\bullet}] \tag{3.3.5}$$

D_o is the oxygen self diffusion coefficient, and $D_{V_o^{\bullet\bullet}}$ represents the oxygen vacancy self diffusion coefficient. $D_{V_o^{\bullet\bullet}}$ is independent of $[V_o^{\bullet\bullet}]$ for moderate concentrations of oxygen vacancies. Hence D_o is proportional to $[V_o^{\bullet\bullet}]$ under this condition.

Also the ionic conductivity σ_i, which is usually $<< \sigma_e$ in acceptor doped perovskites, may be calculated by measured oxygen flux data. Therefore, the integrated Wagner equation. is rearranged to:[2]

$$\sigma_i = J_{O2} \times \frac{4^2 F^2 L}{RT \times (lnP_1 - lnP_2)} \tag{3.3.6}$$

Further important for fast oxygen transport is that all vacancies are available for the diffusion process and not ordered like in the brownmillerite type which can be generated from oxygen deficient perovskite as described in the previous section.[1,2]

3.4 Oxygen surface exchange

Since current research is focused on improving the oxygen flux through MIEC membranes, thickness shall be kept under L_c. The reaction mechanism of the oxygen surface exchange shown in section 3.2, Eq. 3.2.3. ten Elshof et al. have shown that the permeated (secondary) side of a membrane offering the lower p_{O2} value is rate determining.[20] This means that the reduced side of the membrane is rate controlling. This fits well with practical results of Gurauskis et al., who showed an surface area increase on the permeate side to strongly increase the oxygen flux.[13] Furthermore, Chang et al. reported about structuring thin membranes only on secondary side or on primary side and concluded the active area on the secondary side to be rate determining.[38]

Oxygen surface exchange is characterized as oxygen flux into or out of the material (oxidation in or reduction out). If the material is in equilibrium the surface exchange fluxes into and out of the material are equal and thus the net oxygen flux is zero. This is referred to be the balanced exchange rate ($j_{ex}^0 = j_{red} = j_{ox}$ at equilibrium condition). Changes in the oxygen partial pressure and thus the chemical potential μ cause a net flow of oxygen into or out of the material. This process is described by Eq. 3.4.1:[6,7,20]

$$j_{O2} \equiv j_{ox} - j_{red} = j_{ex}^0 \times \frac{\Delta\mu_{O2}}{RT} \qquad (3.4.1)$$

Here, j_{ox} and j_{red} represent the oxygen flux into and out of the material and $\Delta\mu_{O2}$ is the chemical potential change of molecular oxygen across the surface. The chemical potential change is given by the Gibbs energy difference for the reaction shown in section 3.2 Eq. 3.2.3 with doubled coefficients:[6,35]

$$\Delta\mu_{O2} \equiv \Delta_r G = RT \times ln\frac{Q_{ox}}{K_{ox}} \qquad (3.4.2)$$

Where Q_{ox} is the reaction quotient and K_{ox} the equilibrium constant respectively for the reaction shown in section 3.2, Eq. 3.2.3 with doubled coefficients.

Eq. 3.4.2 clarified that the oxygen flux is related to chemical potential change of molecular oxygen. There are several ways to express this relation. One way is given by concentration difference of atomic oxygen.[7]

$$\Delta c_O = c_{actual} - c_{neweq} \qquad (3.4.3)$$

Here c_{actual} is the actual concentration of atomic oxygen at the membrane surface and c_{neweq} represents the new equilibrium concentration ($t = \infty$) of atomic oxygen at the membrane surface. The oxygen flux is given with respect to the definition of the surface exchange coefficient in Eq. 3.4.4:[7,20]

$$j_{O2} = \frac{1}{2}j_O = \frac{-D_{chem}}{2}\frac{dc_O}{dx}\Big|_{surface} = \frac{k_{chem}\Delta c_O}{2} \qquad (3.4.4)$$

The relation in Eq. 3.4.4 clarifies that the surface exchange of oxygen is governed by the quantities Δc_O and k_{chem} and thus the oxygen flux in the surface exchange regime for a given Δc_O can only be enhanced by increasing the k_{chem} value.

3.5 Sintering

Since all specimens prepared in this study are polycrystalline ceramics they need to be sintered. Sintering is per definition the processes that lead to densification of a compacted green body by means of a heat treatment.[21]

The achievement of the state of minimum free enthalpy is the major driving force of the sintering process. Powders offer a relatively high surface area and thus a high surface energy. During sintering the surface energies and later on the interface energies decrease. At the same time the increasing number of saturated chemical bonds lead to increased mechanical properties. High temperatures are required to enable material transport e.g. by diffusion. An increase of driving forces can be achieved by high energetic milling, sintering under pressure and or reactive sintering (high chemical potential). During the sintering process pore elimination, grain growth, and pore growth take place. The major material transport mechanisms are viscous and plastic flow, diffusion, evaporation and condensation and dissolving and precipitation. Since these mechanisms are dependent on the activation of material transport, e.g. on the diffusion coefficient, they are strongly temperature dependent.

The stronger ions are bond in a crystal lattice, the higher the sintering temperature needs to be. At the same time strong bonds correlate with high melting point. Hence there is a

dependency of the melting point (T_{melt}) and the sintering temperature (T_{sint}). Early experiences have shown, that for oxides $T_{sint} \approx 0.7\text{-}0.8 \ T_{melt}$. But this value is just given as an indication since sintering activity is dependent on the particular powder characteristics and thereby the driving forces.[21]

It was shown that it is not possible to describe sintering of a particular powder with one single mechanism, hence sintering is divided into different stages. Most common it is divided into an early stage, an intermediate stage and a final stage.

The early stage is referred to offer a specimen shrinkage up to 5%. The final stage begins with the changeover of open pore channels to closed porosity. This process takes place at about 5-10% remaining porosity. Assuming a green body with about 30-40% porosity the major part of specimen shrinkage occurs in the intermediate sintering stage. In the final stage the remaining porosity disappears slowly, while with increasing temperature also strong grain growth and unwanted sporadic pore growth appears.[21] A schematic diagram of the densification as function of temperature by steady heating rate is given in Fig. 3.5.
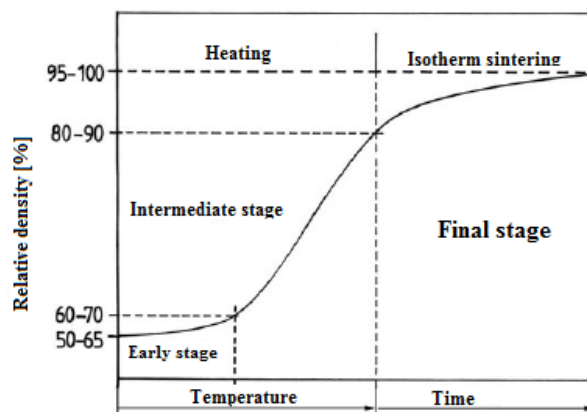
Figure 3.5: Densification process with marked sintering stages[21]

Due to a limitation of T_{sint}, temperature is commonly kept constant in regions of the maximum shrinking rate till the densification of the specimen is sufficient. In the given diagram the temperature axis converts into a time axis while reaching the isothermal holding time.

14

3.6 Porous ceramics

Asymmetric membranes offer a thin active layer and thus need a support to gain structural strength.[3] A route that yields a highly porous ceramics is the addition of a pore forming material which burns off during the sintering process. In literature different pore formers such as corn starch polymeric materials or carbon black were used to obtain sufficient porosity.[12,22,23] In this study, carbon black was used as pore forming agent. Furthermore, the porous support should consist of the same chemical composition to ensure that the onset of shrinking and coarsening are in the same temperature region, and that there is no mismatch in thermal or chemical expansion. Differences in these properties between porous support and the active layer could lead to stresses or fracture formation in the active layer.[23]

The permeability of porous supports is described by the permeability coefficient K [m²/s] using following Eq.3.6.1:[36]

$$K = \frac{\Delta p/_l}{J} \; [\text{m}^2/\text{s}] \tag{3.6.1}$$

Where Δp is the pressure difference across the membrane in, l the membrane thickness, and J the mass flow.[36] Another approach is given by Eq. 3.6.2:[39]

$$D = \frac{\dot{V} \, \eta \, l}{A \, \Delta p} \; [\text{m}^2] \tag{3.6.2}$$

Where $\dot{V}$ is the volumetric flow rate in m³/s, η the dynamic viscosity and A the membrane area. The other characters have the same meaning as in Eq. 3.6.1. Permeability values calculated according to this equation are commonly presented in nano-Perms.

1 nPm = $1*10^{-13}$m². Also the unit Darcy is quite common, where 1 Darcy = 9.872 nPm.[39]

3.7 Deposition techniques

There are several methods known to deposit a functional layer onto a porous support. E.g. sol-gel processing, gas phase techniques, spray deposition technique, sputtering, electrochemical vapor deposition, slip casting, screen printing, spin coating or tape casting and lamination.[22,23] In this study functional layers were deposited by a dip coating technique developed by Gurauskis et al.[12] It was shown that this simple and cost effective technique gives homogeneous, geometry independent, dense layers with a reproducible thickness. To avoid critical failures in the layer small particles with a narrow particle size distribution should be used. This is realizable by colloidal stabilization using dispersion agents.[12]

To obtain surface modification on the functional layer it can be mechanically abrased, a porous layer can be added on top, or it can be etched.[12,25,26,38] In this project membranes were etched by means of wet chemical etching after sintering process, using a method described by E.T. Wefring and D. S. Lagergren.[25,26]

4 Experimental

4.1 Chemicals and Apparatus

All chemicals used in this study including purity and manufacturer are given in the following Tab. 4.1. Tab.4.2 shows all apparatus used for sample fabrication and analysis.

Table 4.1: Chemicals including purity and manufacturer

Chemical	Molecular formula	Purity	Manufacturer / Supplier
LSFAl 2882	$La_{0.2}Sr_{0.8}Fe_{0.8}Al_{0.2}O_{3-\delta}$	$\geq$ 98.5 wt-%	Ø. F. Lohne
Activated charcoal	C	$\geq$ 98 wt-%	Merck KGaA
Reagent grade ethanol	C_2H_6O	$\geq$ 99.8 vol-%	VWR International / Sigma Aldrich
Ethyl cellulose	$C_{20}H_{38}O_{11}$	-	Sigma Aldrich
Hydrochloric acid	HCl	37 wt-%	VWR International
Dolacol D1003	Polymer with ester groups	40% rest solvent	Zschimmer & Schwarz GmbH
Oxygen 5.0	O_2	$\geq$ 99.999%	Yara Praxair
Helium 5.0	He	$\geq$ 99.999%	Yara Praxair
Harmix 5	5% H_2 95% Ar	$\geq$ 99.99%	Yara Praxair
Harmix 10	10% H_2 90% Ar	$\geq$ 99.99%	Yara Praxair
Oxygen calibration gas 0.01	0.01% O_2 1% N_2 rest Ar	$\geq$ 99.999%	Yara Praxair
Oxygen calibration gas 0.1	0.1% O_2 1% N_2 rest Ar	$\geq$ 99.999%	Yara Praxair
Oxygen calibration gas 1	1% O_2 1% N_2 rest Ar	$\geq$ 99.999%	Yara Praxair
Hydrogen calibration gas 0.1	0. 1% H_2 1% N_2 rest Ar	$\geq$ 99.999%	Yara Praxair
Hydrogen calibration gas 1	1% H_2 1% N_2 rest Ar	$\geq$ 99.999%	Yara Praxair

Table 4.2: Apparatus and application

Apparatus	Application
Bruker AXS D8 Focus	X-ray diffractometer (XRD)
NETSCH STA 449C	Thermo gravimetric-analysis (TGA)
NETSCH DIL 402C	Dilatometer-analysis (DIL)
Hitachi S-3400N LV -SEM	Scanning electron microscope (SEM)
Oxford Instruments X-Max	Energy dispersive X-ray spectroscopy (EDS)
Micromeritics Tristar^{TM}3000	Nitrogen Adsorption (BET)
Malvern Mastersizer 2000	Particlesizer (Dynamic light scattering)
Mars III Haake	Rotational rheometer
Buchi Rotavapour	Rotary evaporator
Branson Digital Sonifier	Ultra sonic finger
Nabertherm P 330	Calcination and sintering furnace
Entech HT-2	Sintering furnace
Varian Micro-GC CP4900	Gas chromatograph

4.2 Procedure

4.2.1 Phase determination

Powders and specimens were checked for phase purity by means of X-ray diffraction. All illustrated XRD patterns were measured on a Bruker D8Focus working in Bragg–Brentano ($\Theta/2\Theta$) geometry. XRD data of powder and sintered samples were measured from $2\Theta = 10$–$80°$ (step size $0.02°$ and integration time 0.15 s) using CuK_α radiation. A cubic reference diffraction pattern ($La_{0.2}Sr_{0.8}FeO_{3-\delta}$ entry number 1404417) offering a lattice constant of 3.8643 Å was taken from Pearson's crystal data base.[31]

4.2.2 Particle size distribution and surface area determination

Particle size distribution was measured according to the principle of dynamic light scattering (DLS) on a Malvern Mastersizer 2000. Refractive index was set to default (1.52). A proper amount of the powder or suspension was dispersed in distilled water. The amount of powder or suspension was monitored by the software. Prior to measuring and during measuring the dispersion was stabilized by stirring and ultra sonication. The software measured each sample four times and calculates the average particle size distribution.

Surface area was measured by means of nitrogen adsorption (BET) on a Micromeritics Tristar^{TM}3000. Approximately 1-2 g powder were fed into a weighed BET tube and degassed at 250 °C for 24 h. After de gassing the accurate powder mass was evaluated by weighing the dried powder.

4.2.3 Thermo gravimetric analysis

Burn off of carbon black was observed by TGA on a NETSCH STA 449C. TGA was performed with a heating rate of 2 K/min to 1000 °C and a cooling rate of 4 K/min to room temperature in synthetic air.

4.2.4 Linear shrinkage

Linear shrinking behavior was analyzed via dilatometry using a NETSCH DIL 402C. Heating rate was set to 2 K/min up to 1300 °C in synthetic air. Specimens for dilatometry were produced by dye pressing at 40 MPa for 2 min. Specimen dimensions were approximately Ø 5 mm and 5 mm in height.

4.2.5 Suspension viscosities

Rheological behavior of the 2 vol-% solid load containing suspensions was analyzed with a rotational rheometer Mars III (Haake, Karlsruhe). The rheometer was equipped with double cone-and-plate test geometry (titanium double cone of 1°, $\emptyset = 60$ mm). Approximately 5 ml of each suspension were sheared up to a shear rate of 500 s^{-1} in controlled share rate (CR) mode. Dwell time was set to 30 s at the maximum shear rate and then sheared down again. Temperature was kept constant at 20 ± 0.1 °C.

4.2.6 Density and porosity determination

Green body densities were measured by geometric means. Assuming the green bodies to be ideal cylinders their weight and dimensions were measured and the density was calculated using the cylindrical volume formula and the green body mass.

Densities and open porosities of ceramic disks and porous supports were determined according to Archimedes principle (ISO 5017:1998(E))in iso-propanol. The theoretical (X-Ray) density of $La_{0.2}Sr_{0.8}Fe_{0.8}Al_{0.2}O_{3-\delta}$ was communicated by PhD student T.N. Phung of University of Twente to be 5.54 g/cm^3.[32]

Fundamental data for ceramic disks is the bulk density in gram per cubic centimeter or in percentage of the theoretical density value. For porous supports the fundamental data is the apparent (open) porosity expressed as percentage of the bulk volume.

4.2.7 Scanning electron microscopy / Energy dispersive X-ray spectroscopy

SEM micrographs were made on a Hitachi S-3400N LV -SEM using a Rhodium electron source with SE and BSE detector. Applied voltages were 10, 15 and 20 kV.

Ceramic samples were attached to the sample holder using tacky carbon tape, powder were dispersed in ethanol, directly contacted to the sample holder and dried. Further gold or carbon coating is not necessary since the material is conductive. Furthermore, degradation studies were made using BSE images and attached Oxford Instruments X-Max EDS system.

4.2.8 Permeability measurements

The measurement setup used to measure oxygen permeation has been established by Gurauskis et al.[13]

The oxygen permeation was measured using a Varian Micro-GC CP4900 gas chromatograph as function of the oxygen partial pressure in a permeation furnace. This tube furnace consists of an outer (Ø 45.25 mm) and inner (Ø 16.2 mm) alumina tube which are both separateable. The inner tube is on both sides connected to gas in and outlets like illustrated in Fig. 4.1b). The Asymmetric and disk shaped membranes were mounted in an intermediate alumina house offering an inner diameter of 16.60 mm, and sealed like illustrated in Fig. 4.1a) using gold as sealing agent.
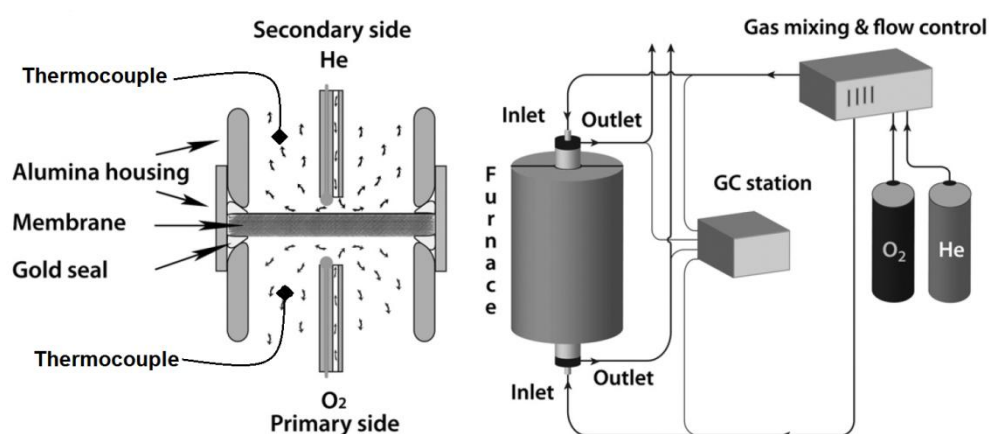
a) Schematic illustration of a membrane fitting   b)gas supply and evaluation arrangement

Figure 4.1: Experimental setup for oxygen permeation measurements [13]

For sealing the membranes were located between two gold rings and slowly heated up to 1055 °C. This temperature is close to the melting point of gold. At this temperature a load was put on top of the flux furnace, to generate pressure and thereby create a tight interface between the membrane and the softened gold.

Active membrane area was 1.05 cm². Changes in oxygen partial pressure were realized by changing the helium flow rate on the permeate (secondary) side (6 - 860 ml/min) while the oxygen flow on the primary side was kept constant at 100 ml/min. The total pressure was set to atmospheric pressure on both sides. Temperature accuracy was monitored by reference thermocouples located close to both sides of the membrane. All permeation measurements were carried out in the range from 800 °C to 1000 °C. Between each measurement the system was left an accurate time (4-6 h) for conditioning. The oxygen concentration on the secondary side (in the helium sweep) was detected by the GC station equipped with a M5A#BF column of 10 m length and a thermal conductivity detector. Argon was used as carrier gas. After measurements were completed the membranes were exposed to 5% hydrogen 95% argon gas mixture for 100 h at 900 °C and a flow rate of 128.68 ml/min. During exposing the oxygen flux was measured indirectly, by measuring the hydrogen concentration in the exhaust. Since oxygen reacts with hydrogen under water formation the oxygen concentration and thus the oxygen flux can be calculated by determining the hydrogen consumption. Afterwards the sweep was changed to helium again, and conditioned for 24 h. Oxygen flux was remeasured to check degradation in the flux values. Asymmetric membranes were also exposed to 10% hydrogen containing gas mixture for 100 h since during exposing to 5% hydrogen no hydrogen was detectable by the GC. Calibration of the GC system was performed using oxygen and hydrogen reference gasses and possible leakages were determined by monitoring (GC) the primary membrane side (Oxygen exhaust) for helium. The calibration curves for oxygen and hydrogen are shown in Fig. 4.2. Since hydrogen values were just measured once, accuracy bars cannot be included.
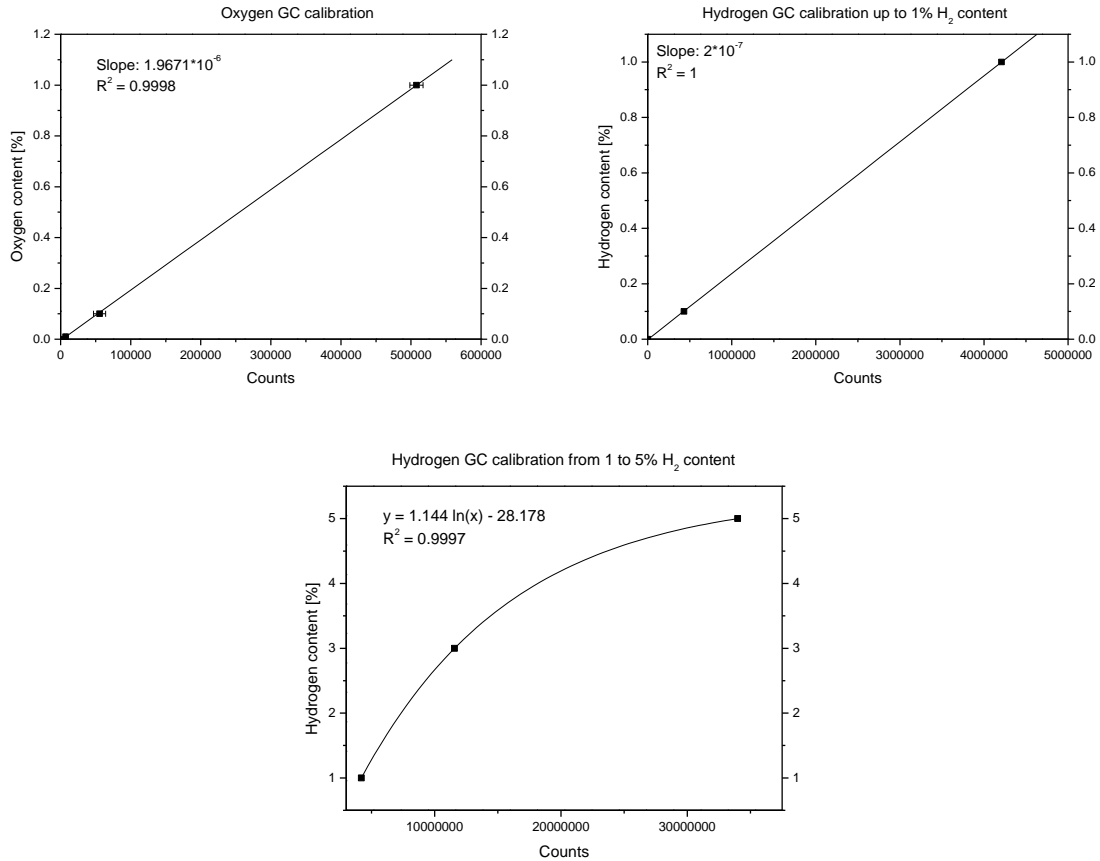
Figure 4.2: GC calibration curves for oxygen and hydrogen

4.2.9 Powder preparation

LSFAl 2882 powder received for this project was produced by Ø. F. Lohne using spray pyrolysis. Therefore, stoichiometric amounts of $Sr(NO_3)_2$ (Sigma Aldrich ACS reagent $\geq 99.0\%$), $Fe(NO_3)_3 * 9H_2O$ (Sigma Aldrich ACS reagent $\geq 99.0\%$), $Al(NO_3)_3 * 9H_2O$ (Merck p.a. $\geq 98.5\%$) and La^{3+}(EDTA) ($La(NO_3)_3 * 6H_2O$ Metall Rare Earth Limitied 99%. EDTA Sigma Aldrich) were mixed, stirred for homogenization and finally spray proylized at 1000 °C with a feed rate of 10 L/h. After spray pyrolysis the powder precursor was mortared and calcined at 900 °C for 12 h in air with a heating and cooling rate of 200 °C/h.

The received powder was checked for phase purity by means of XRD. Afterwards powder was fed into a 500 ml polyethylene bottle covered with the same amount of alumina grinding balls (Ø 5 mm) and wetted with reagent grade ethanol to form a slurry. This was ball milled

for 24 h at an approximately rotation speed of 100 rpm. After ball milling the grinding media was removed, the slurry was dried in a rotation evaporator and finally mortared and sieved to 250 μm. Particle size distribution, surface area and morphology were characterized by DLS, BET and SEM.

4.2.10 Preparation of ceramic disks

Ceramic disks were prepared "the classical" way of dye pressing and sintering. Approximately 1 g LSFAl 2882 powder was fed into a 25 mm Ø double side pressing dye and uniaxially pressed for 2 min with a pressure of 40 MPa. Green body density was measured and the green bodies were sintered at 1100 °C (1 h, hr 120 °C/h, cr 60 °C/h), 1200 °C (2 h hr 120 °C/h, cr 100 °C/h to 1000 °C then 30 °C/h),and 1230 °C (2 h hr 120 °C/h, cr 100 °C/h to 1000 °C then 30 °C/h) in air. Sintering programs are illustrated in Fig. 4.3. After sintering final densities were determined by Archimedes method (ISO 5017:1998(E)) and morphology was investigated by SEM.
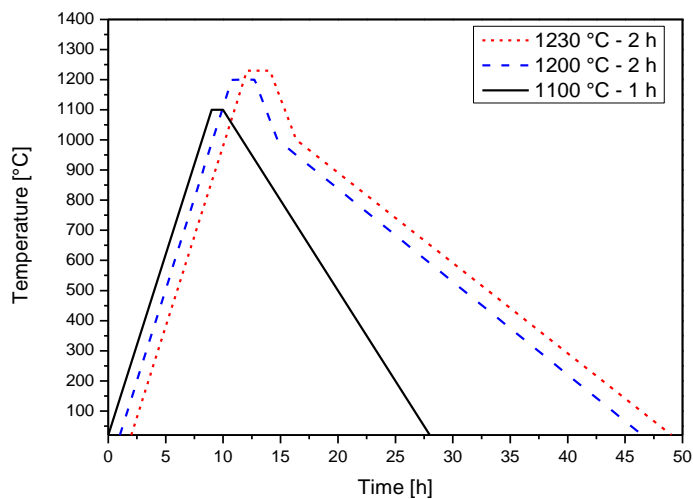
Figure 4.3: Sintering programs of LSFAl 2882 disks

4.2.11 Preparation of porous supports

To achieve a porous support for asymmetric membranes LSFAl 2882 powder was mixed with 30 wt-% carbon black addition. This corresponds to ~42 vol-% of the mixture. The powder mixture was fed into a 250 ml polyethylene bottle and covered with the same amount of alumina grinding balls (Ø 5 mm). To achieve a slurry reagent grade ethanol was added till the components were completely covered. Powder composition is given in the following Tab. 4.3.

Table 4.3: Composition of porous LSFAl 2882 powder mixture

Chemical	Amount [g]	Amount [wt-%]	Amount [vol-%]
LSFAl 2882	10	76.92	57.63
Carbon black	3	23.08	42.37
Mixture	13	100	100

The slurry was ball milled for 1 h for homogenization, afterwards the grinding media was removed and the slurry was dried in a rotation evaporator. The powder mix was then mortared and some reagent ethanol was added to form a thick slurry. 3 wt-% ethyl cellulose binding media was added to the slurry. For homogenization of the binding media the slurry was mortared for 15 min and dried over night.
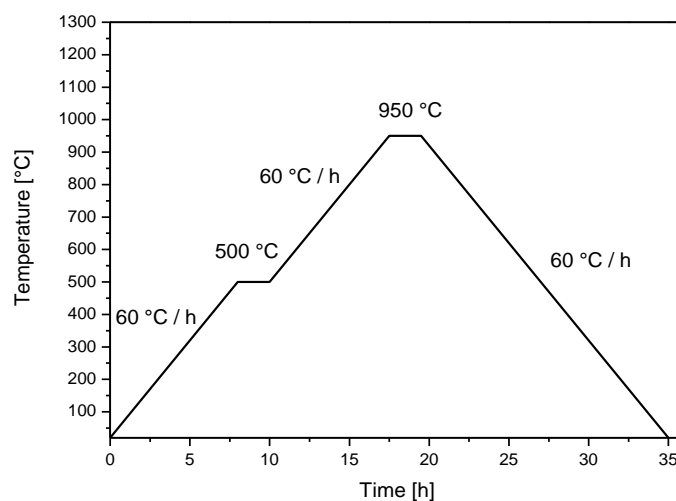
Figure 4.4: Calcination program for porous supports

Approximately 2 g powder mixture was fed into a Ø 25 mm double side pressing dye and uniaxially pressed for 5 min with a pressure of 40 MPa. Green density was measured and the porous supports were calcined at 950 °C for 2 h in air.

The calcination program is given in Fig. 4.4. Slow heating rate and dwell step at 500 °C is to ensure a slow burn off of carbon black without destroying the support. After calcination the density of the supports was determined again.

4.2.12 Stabilized LSFAl 2882 suspensions

To ensure that dip coating results in a homogeneous layer, stable suspensions need to be fabricated. The surfactant used for stabilizing is DOLACOL D 1003, the dispersion media reagent grad ethanol. For determination of the optimal surfactant amount 5 different suspensions were prepared all containing 2 vol-% solid load. The surfactant content was set to 1.5, 2, 2.25, 2.5 and 3 wt-% and was mixed 1 to 10 with reagent grade ethanol to ensure sufficient masses prior to weighing. The mixing parameters are given in the following Tab. 4.4.

Table 4.4: Suspension components

Component	1.5 wt-% Surfactant content	2 wt-% Surfactant content	2.25 wt-% Surfactant content	2.5 wt-% Surfactant content	3 wt-% Surfactant content
LSFAl 2882 [g]	2.5	2.5	2.5	2.5	2.5
Ethanol [g]	17.131	17.018	16.962	16.906	16.793
Dolacol D 1003 (1/10) [g]	0.375	0.5	0.563	0.625	0.75
Total [g]	~20	~20	~20	~20	~20

Mixed suspension were transferred into 50 ml polyethylene bottles, filled with approximately the same volume of alumina grinding balls (Ø 5 mm) and ball milled for 24 h at a rotation speed of 170 rpm. The viscosity of the final suspension was analyzed and the particle size distribution was measured.

Gurauskis et al achieved dense defect free layers using a suspension containing 0.5 vol-% solid load.[12] Hence the same solid load was used in this project for the dip coating process. The fabrication is illustrated in the following flow chart (Fig. 4.5).

Mixing 2.5 g LSFAl 2882, 16.962 g Ethanol, 0.563 g Surfactant (1/10 diluted) and the same volume amount Alumina grinding media (Ø 5 mm) in a 50 ml polyethylene bottle.

24 h ball milling at a rotation speed of 170 rpm

Diluting the suspension 1/4 with reagent grade ethanol in a 250 ml polyethylene bottle to contain 0.5 vol-% solid load.

Constantly slow rolling for further stabilization

1 min ultra-sonication on an amplitude of 15% prior to dip coating

Figure 4.5: Summary of the suspension fabrication

4.2.13 Preparation of asymmetric membranes

For the dip coating process calcined porous supports were attached to glass plates, using liquid latex, to limit the deposition of the dense functional layer to one side. After the liquid latex was solidified the stabilized LSFAl 2882 suspension was ultra-sonified as described before to ensure randomly distributed particles and to avoid sedimentation. The suspension was transferred to a small polystyrene container and a functional layer was deposited on the porous support by dipping it into the suspension for 5 s. The first membranes were directly pre-sintered after this single dip-coating, but later on membranes were kept to dry for 10 min and then dip coated again for 5 s. (double dip coated).

After dip coating membranes were dried for 2 h at room temperature, carefully removed from the glass plates and pre sintered at 1100 °C for 1 h in air. The pre-sintering program is given in Fig. 4.6.
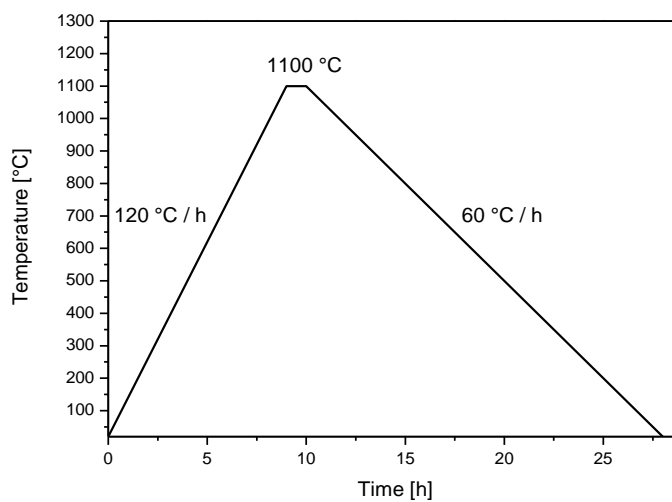
Figure 4.6: Pre-sintering program for asymmetric membranes

After pre-sintering membranes were attached to glass plates again and dipped one more time using same parameters as before to support gas tightness. Fig. 4.7 shows a pre-sintered membrane attached on a glass plate for dip coating.
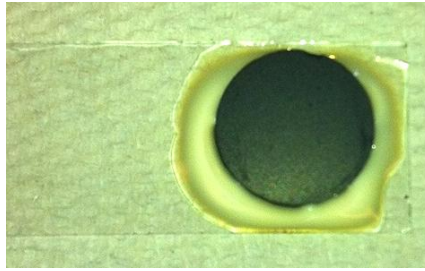
Figure. 4.7: Pre-sintered membrane prepared for dip coating

After final dip coating and drying membranes were sintered at 1175, 1200 and 1230 °C for 2 h with a dwell of 2 h, a heating rate of 120 °C/h and a cooling rate of 60 °C/h, in air, as illustrated in Fig. 4.8.
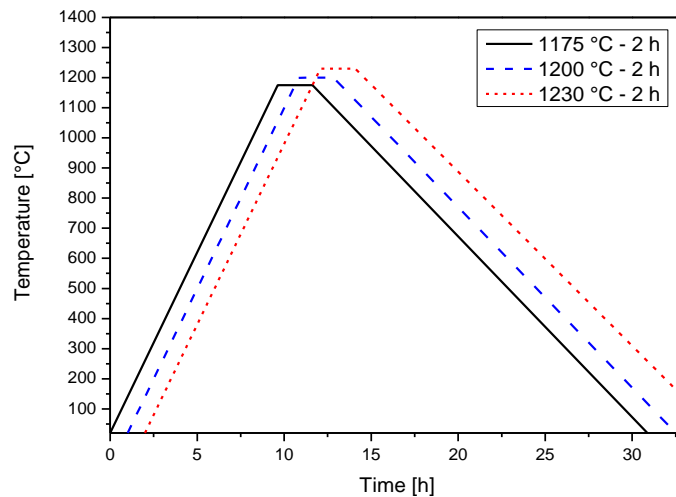
Figure 4.8: Sintering programs for asymmetric membranes

Layer density, thickness and porosities of the supports were investigated by SEM and final membranes for permeation measurements were triply dip coated and sintered at 1230 °C.

4.2.14 Surface structuring

Surface structuring was done by means of wet chemical etching using HCl as etchant. D.S. Lagergren reported that 6 M HCl gave best results for a similar composition (LSFTa 2882) thus it was used for etching LSFAl 2882.[26] For the etching process membranes were attached to glass plates using liquid latex. Also a part of the surface was covered with liquid latex to keep the surface at the outer regions smooth. This was done to ensure proper sealing in the permeation furnace. After the liquid latex was dried the membranes were put into a beaker filled with 50 ml 6 M HCl for 1.5, 4 and 5 min. Temperature of the HCl bath was 22 °C and the pH was measured to be 0. After removing from the beaker, membranes were intensively washed under flowing water and ethanol. The surface structuring was investigated by SEM.

5 Results

5.1 Characterization of the powder precursor

LSFAl 2882 powder received for this project was spray pyrolyzed and calcined at 900 °C for 12 h. Calcination was done according to TGA analysis. Fig. 5.1 shows the mass loss plotted against temperature of the raw LSFAl 2882 precursor prior to calcination.
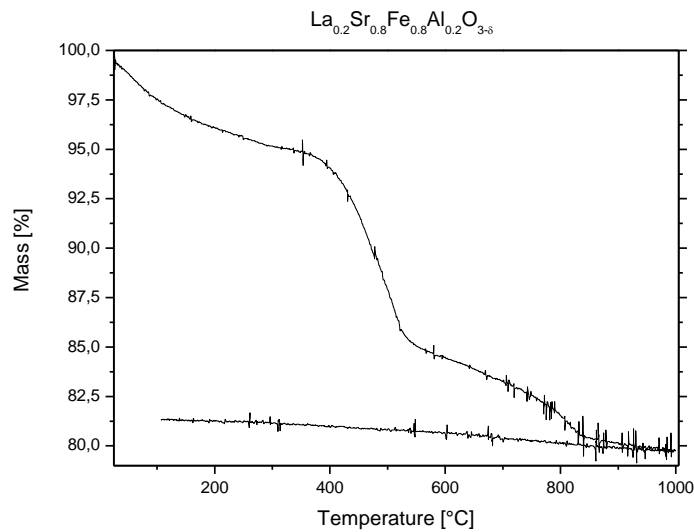
Figure 5.1: Mass loss of the raw LSFAl 2882 powder precursor

From the TGA plot it is evident that a mass stability is given at a temperature of about 900 °C after a total mass loss of 20 wt-%. Furthermore, three regions are apparent. The main loss of mass up to 100-150 °C is due to water evaporation overlapping with crystal water leaving the system. At temperatures from 350 °C up to 550 °C the mass loss is governed by the decomposition of nitrates and EDTA-complexes remaining from the spray pyrolysis process. In the temperature region over 550 °C carbonates start to decompose. After calcination the phase purity of the LSFAl 2882 powder was checked by XRD. The normalized XRD pattern is given in Fig. 5.2. with a $La_{0.2}Sr_{0.8}FeO_{3-\delta}$ reference from Pearson Crystal Database (1404417).[31] Fig. 5.2 shows that the sample is single phase and cubic perovskite structured.
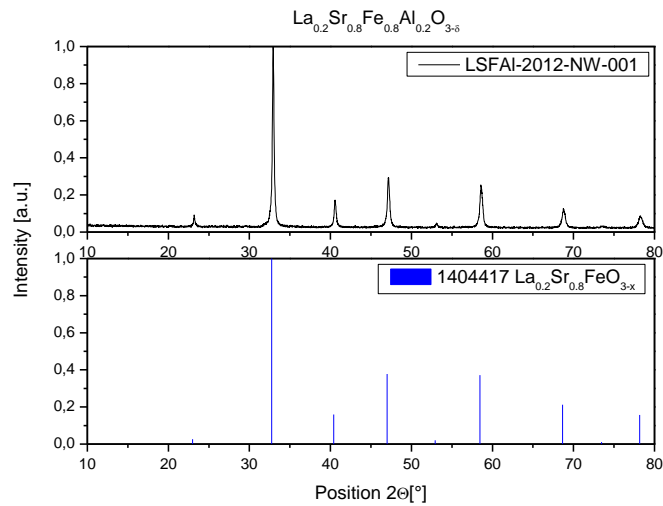
Figure 5.2: XRD pattern of LSFAl 2882 powder with given reference

The morphology of the phase pure powder was characterized with SEM. Micrographs illustrated in Fig. 5.3 show typical spherical or hollow spherical agglomerated particles resulting from spray pyrolysis process at different magnifications.
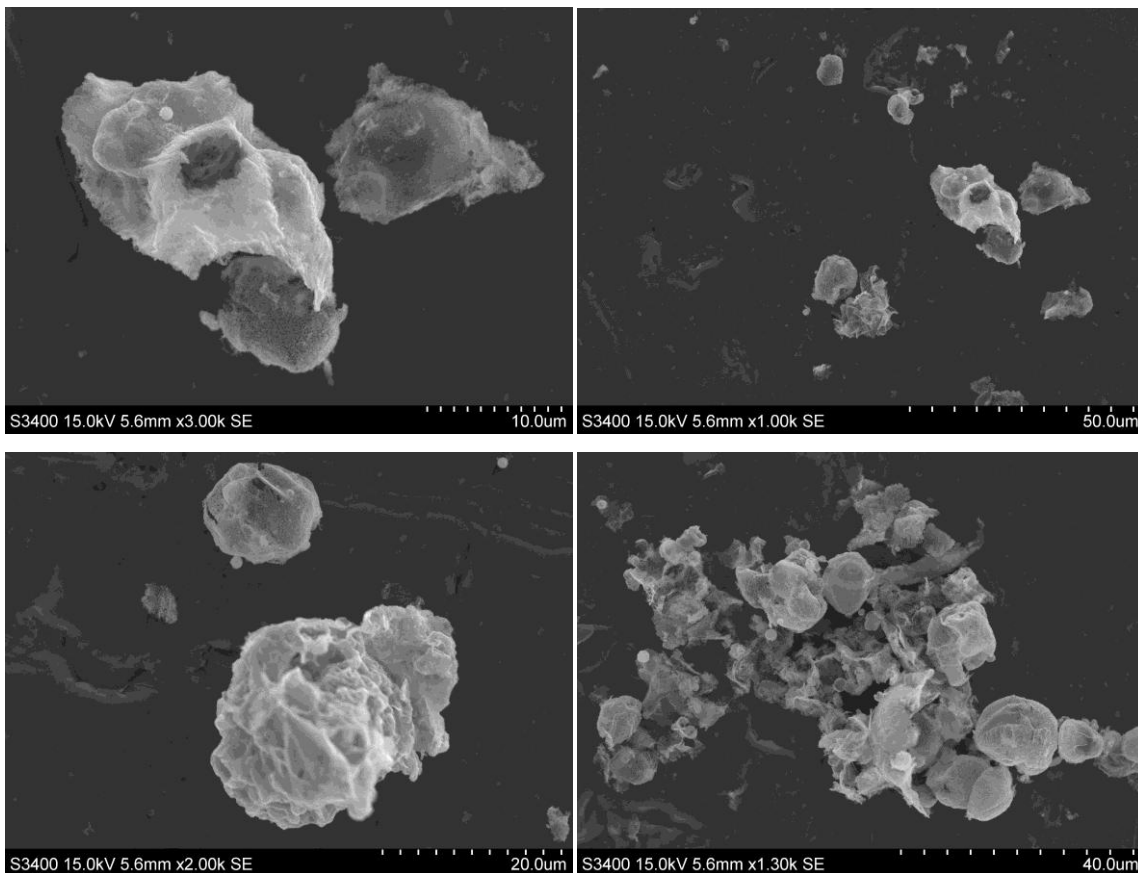
Figure 5.3: SEM micrographs of LSFAl 2882 powder at different magnifications

Since this particle shape is not suitable for dense ceramic fabrication the powder was ball milled as described in the previous section. Resulting powder was characterized by BET, DLS and SEM. BET gave a surface area of 10.1815 ± 0.0525 m²/g. That corresponds to primary particles of 106.4 nm assuming that they are spherically shaped. The particle size distribution measured according to the principle of DLS is illustrated in Fig. 5.4.
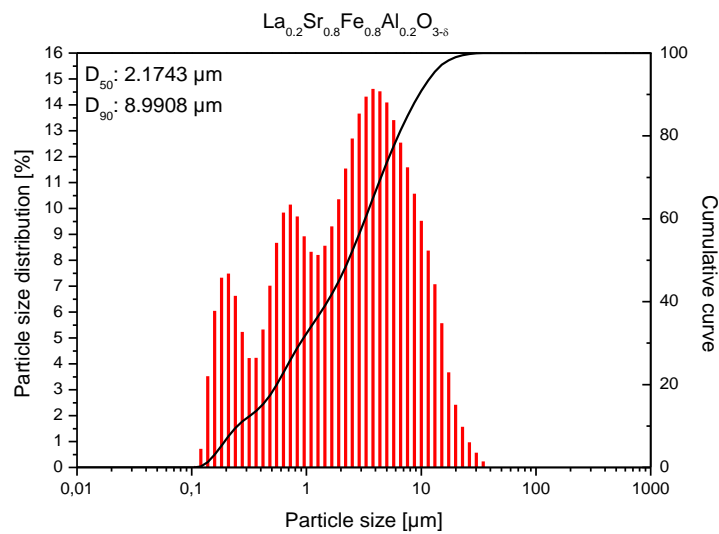
Figure 5.4: Particle size distribution of ball milled LSFAl 2882 powder

The particle size distribution is tri modal and offers a d_{50} value of 2.17 μm. The first peak at 150-200 nm fits quite well to the calculated BET value and thus corresponds to the primary particle size. While the second and third peaks correspond to the presence of agglomerates. From the d_{50} value it is clear that a huge amount of the LSFAl 2882 powder is still agglomerated after ball milling.

Also results from SEM analysis confirm these values. Fig. 5.5 shows micrographs of ball milled powder.
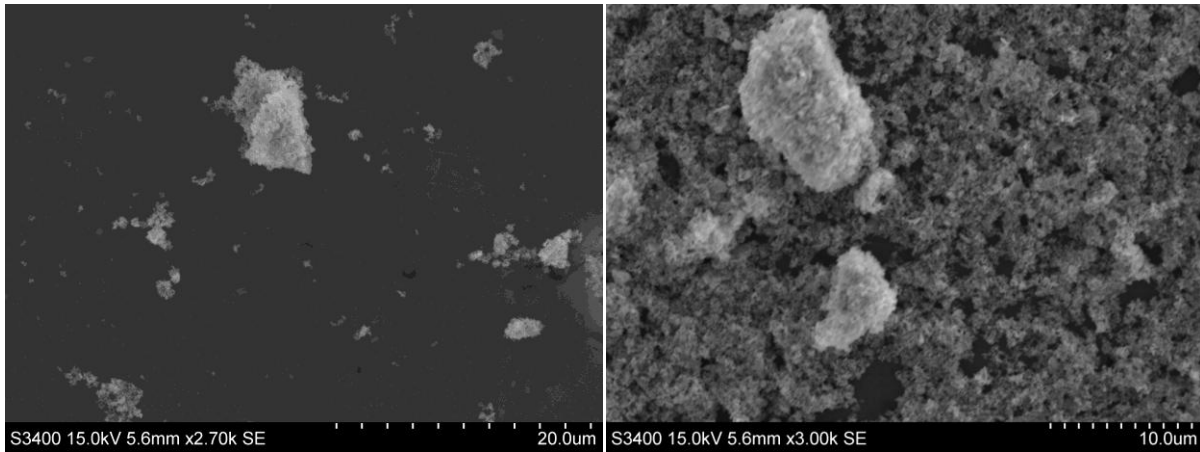
Figure 5.5: SEM micrographs of ball milled LSFAl 2882 powder

Sub-micron sized particles are apparent next to larger agglomerates. This is especially visible in the right micrograph of Fig. 5.5. Here two big agglomerates are lying on top of a powder bed consisting of particles in the sub-micron range.

Linear shrinkage of the powder was analyzed by dilatometry to gain information about the sintering behavior of LSFAl 2882. Fig. 5.6 shows the dilatometer analysis of LSFAl 2882 including the first derivative.
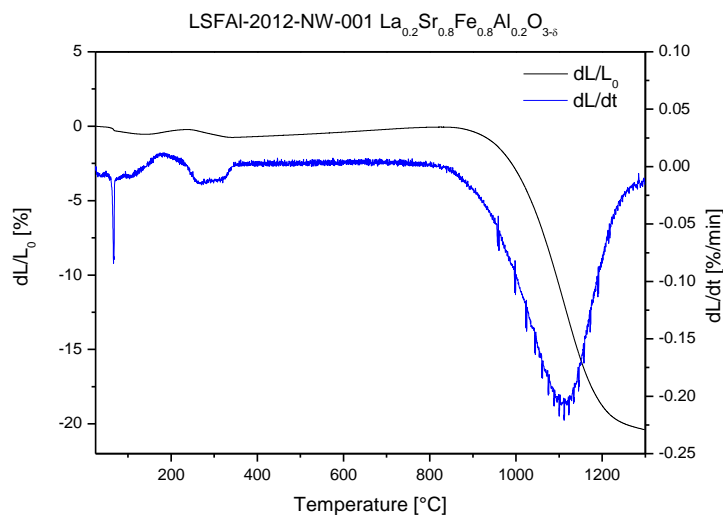
Figure 5.6: Dilatometer analysis of LSFAl 2882 including time program and first derivative (Heating rate 2 °C/min)

Densification of the powder starts at about 900 °C and the maximum rate of densification according to the derivative is at 1100 °C.

5.2 Shaping and sintering of ceramic disks

Parameters of the prepared green bodies given exemplary in the following Tab.. Approximate dimensions of green bodies were Ø 25 mm and 1 mm height.

Table 5.1: Green body parameters

Mass [g]	Diameter [mm]	Height [mm]	Density [g/cm³]	Theoretical density [g/cm³][32]	Percentage of theoretical density [%]
1.0495	25.06	0.96	2.216	5.54	40

Taking dilatometer data presented in the previous section into account a first estimate for sintering was 1100 °C. Since densities were not sufficient, samples were sintered at 1200 °C and 1230 °C using the furnace programs illustrated in section 4.4. The cooling rate from 1000 °C to room temperature was set to 30 °C/h since samples cooled faster suffered fractures. Resulting densities are plotted in Fig. 5.7.
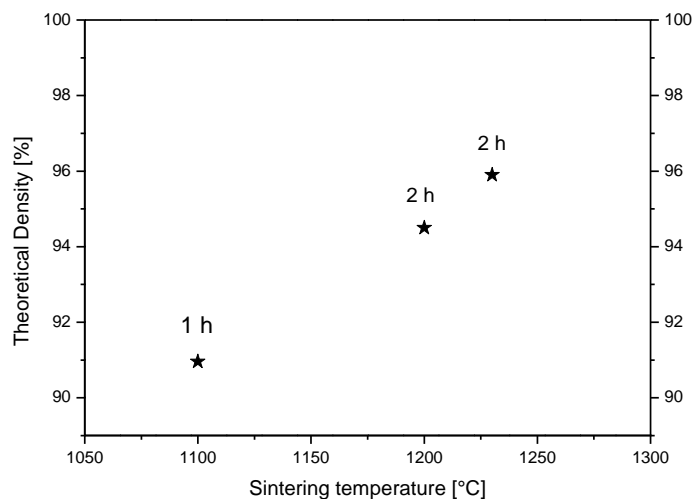
Figure 5.7: Densities of ceramic disks depend on the sintering temperature

Densities of approximately 96% of the theoretical density were reached at a sintering temperature of 1230 °C for 2 h. This value is sufficient to guarantee gas tightness since open

porosity was absent, and thus disks for permeation measurements were produced according to this route. Resulting dimension were approximately Ø 17 mm and 0.7-0.8 mm in height.

Furthermore surface and cross section of disks produced according to this route were investigated by SEM. To generate a cross section a disk was broken in a controlled manner using pincers. The following Fig.5.8 shows SEM micrographs of a sintered LSFAl 2882 disk at different magnifications.

| a) Disk surface | b) Disk surface with marked grain dimensions |

| c) Cross section | d) Cross section |
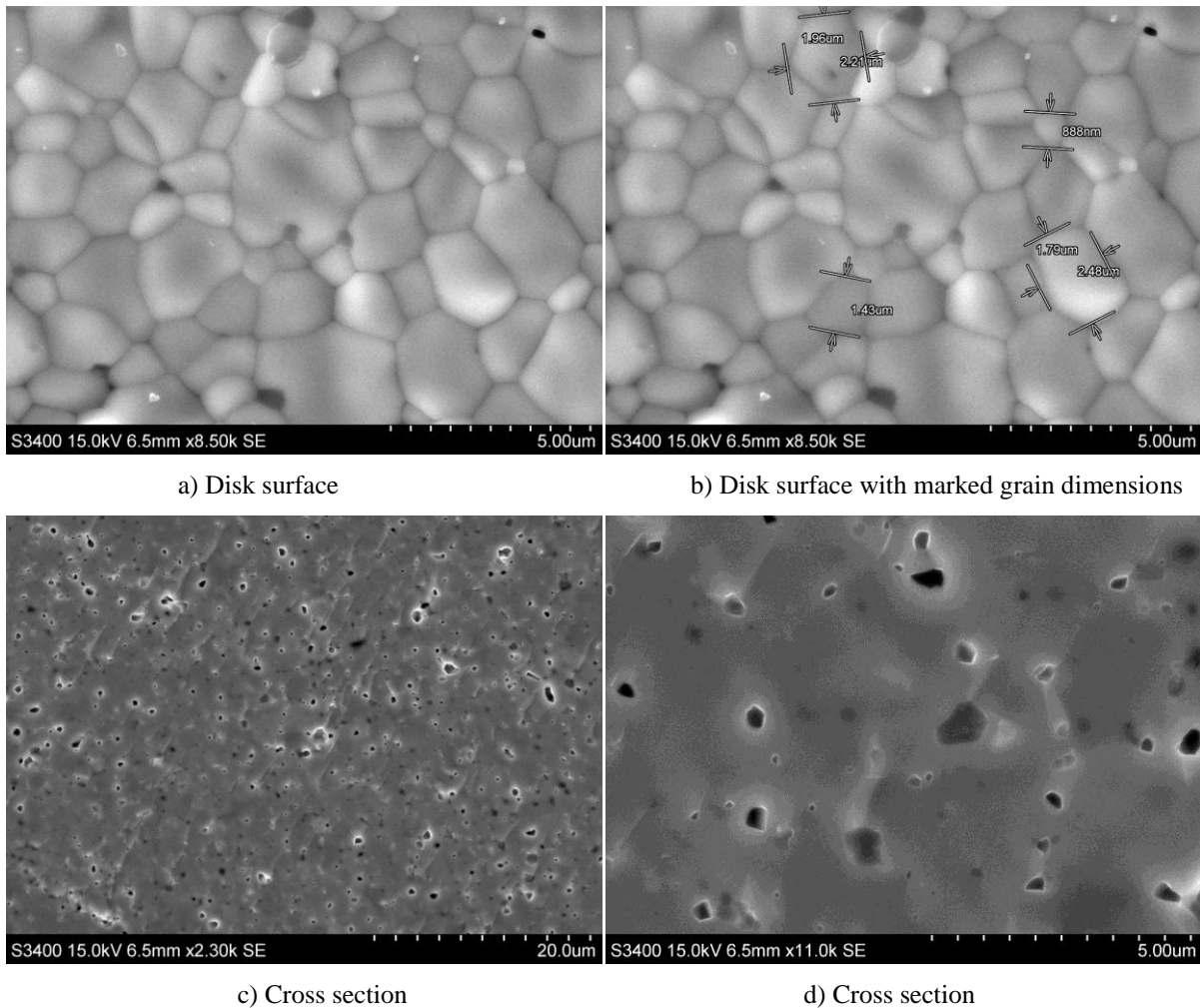
Figure 5.8: Micrographs of a sintered disk surface and cross section on different magnifications

Part b) of Fig. 5.8 clarifies an average grain size of about 1.5 μm and a dense surface. Parts c) and d) showing the remaining pores in the bulk located mostly at grain boundaries.

To ensure phase purity after sintering the disks were analyzed by XRD. In Fig. 5.9 a XRD pattern clarifying single phase, cubic perovskite structured, LSFAl 2882 is illustrated using the same reference as in the previous section.
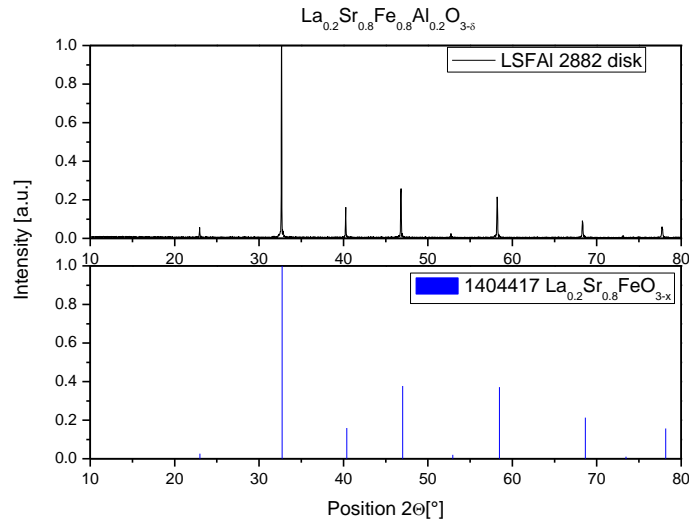
Figure 5.9: XRD pattern of a sintered LSFAl 2882 disk

5.3 Shaping and sintering of porous supports

To ensure that the carbon black pore former burns off in a controlled and slow manner, the temperature dependent mass loss of the LSFAl 2882 CB powder mix was measured with TGA (Fig.5.10).
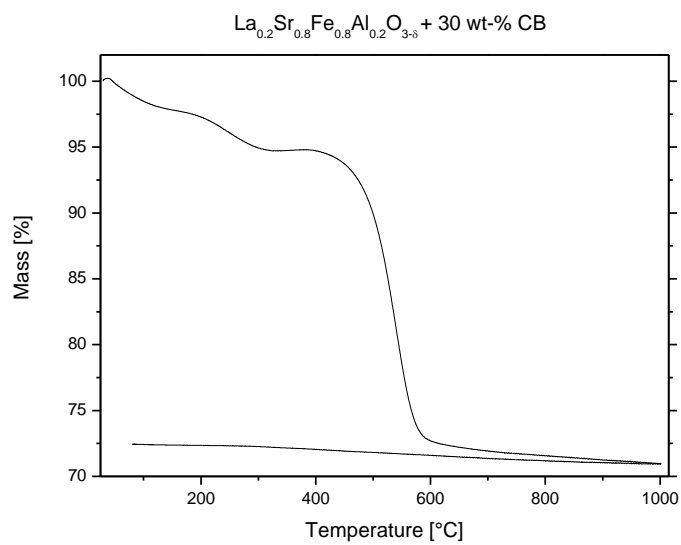
Figure 5.10: Mass loss of the powder mix for porous support fabrication

In the TGA plot two regions are apparent. In the first region up to 300 °C water and the ethyl cellulose binding agent decompose. The second region from approximately 450 °C to 600 °C corresponds to the oxidation of carbon black to CO and CO_2. According to this TGA plot the temperature program shown in section 4.5 was set and the porous support was hold at a temperature of 500 °C for a sufficient time.

Green bodies for porous supports were, like ceramic disks, fabricated by uniaxially dye pressing in a double action dye. Prior to asymmetric membrane production one porous support was pre-sintered and sintered using parameters shown in section 4.5 to ensure stability, porosity and permeability of the supports. Diameters of the supports were approximately 25 mm prior and 16 mm after sintering.

Final density, porosity and green densities of the intermediate steps are shown in Tab.5.2.

Table 5.2: Density and porosity values of porous supports

Condition	Density [g/cm³]	Percentage of theor. density [%]	Porosity[%]	Open porosity [%]	Closed porosity [%]
Green body	1.298	Not available	Not available	Not available	Not available
Calcined	1.015	18.32	81.68	Not available	Not available
Pre-sintered	1.496	27.00	73.00	Not available	Not available
Sintered	2.795	50.45	49.55	47.33	2.22

Since only sintered porous supports were analyzed by means of Archimedes method, open and closed porosity values are just available for sintered supports. A comparison to the theoretical density of LSFAL 2882 (5.54 g/cm³) is not possible for the green body since it is mixed with a lot of carbon black.

Sintered supports offer open porosity values of almost 50%, also SEM micrographs prove a high degree of open and connected porosity of the supports. Furthermore, the morphology of the CB pore former was investigated. All this is illustrated in Fig.5.11.
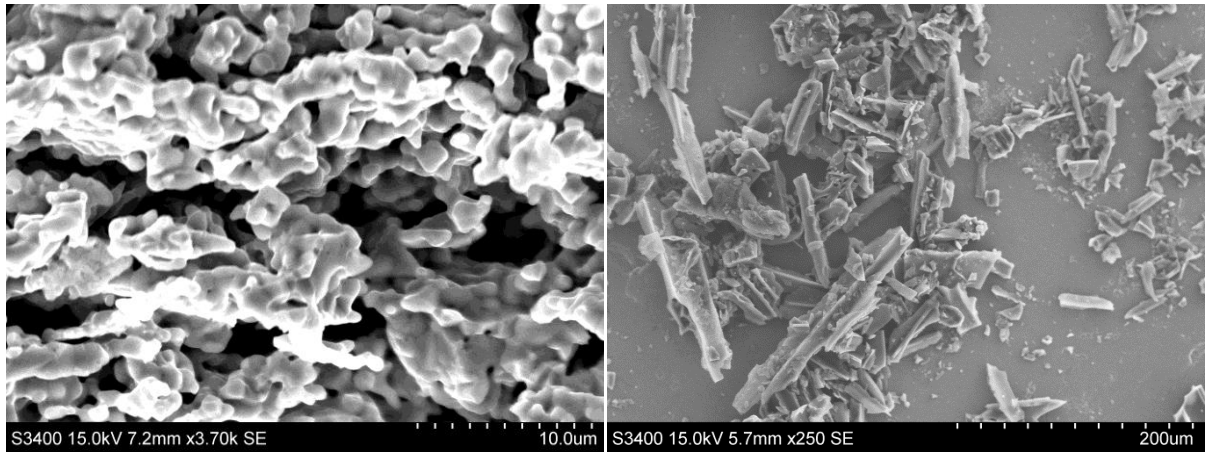
a) Sintered porous support   b) Carbon black pore former

Figure 5.11: SEM micrograph of a porous support and carbon black pore former
(note different magnifications)

Part b) shows the broad variation of particle shape of the CB pore former, hence mixed LSFAl 2882 / CB results in highly porous material as illustrated in part a).

Also the permeability of a porous support was measured and the pressure dependent permeability coefficient K ascertained as function of the mean pressure according to Altena et al.[36] Furthermore, the permeability in nPm and Darcy was calculated. The results is shown in Fig. 5.12.
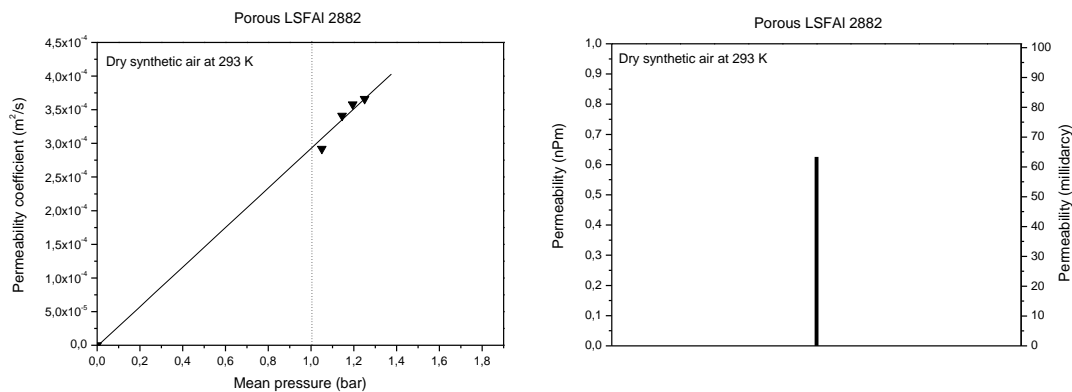
Figure 5.12: Permeability coefficient and permeability of a porous support

5.4 Investigations on stabilized LSFAl 2882 suspensions

To prepare suspensions for dip coating they were mixed with the surfactant DOLACOL D 1003 and ball milled 24 h like described in section 4.6. The particle size distribution of the five stabilized suspensions was measured and is illustrated in Fig. 5.13.
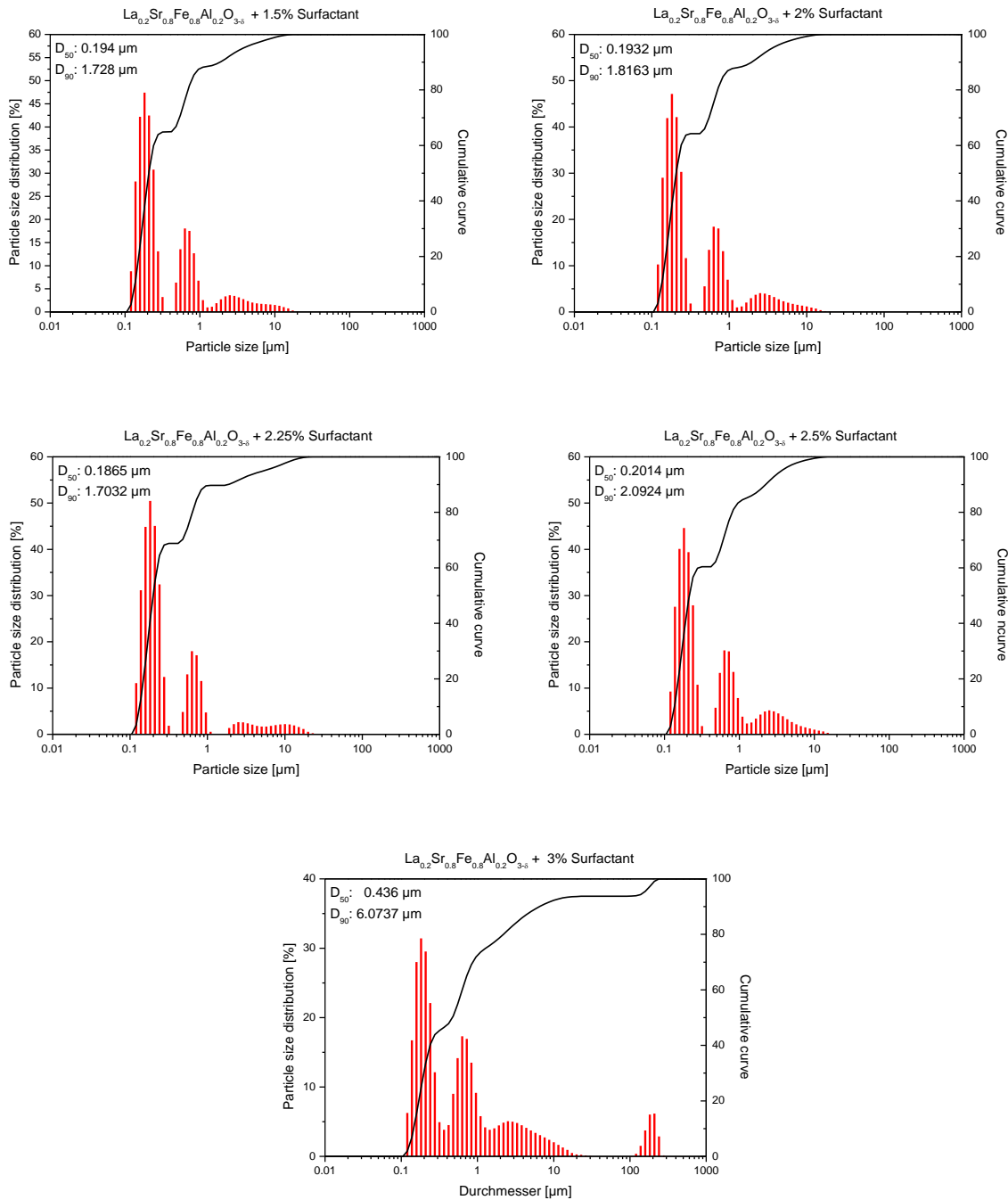
Figure 5.13: Particle size distributions of stabilized suspensions

All particle size distributions look quite similar offering a big amount primary particles in the sub micron range. The d_{50} values of all suspensions beside the one containing 3% surfactant is in the range of approximately 200 nm and the amount of remaining agglomerates is quite low. The appearance of big particles over 100 μm in the suspension containing 3% surfactant is most probably a measurement artifact caused by gas bubbles.

To decide which suspension is most suitable for the dip coating process the viscosity was measured with a rotational rheometer with double cone-and-plate test geometry. Part a) of Fig. 5.14 shows the viscosity dependence on shear rate. The plot in part a) shows the down shearing part of the experiment to ensure mounting errors are excluded. Part b) shows viscosity values at a fixed shear rate of 100,8 s^{-1}. The value for the 2% surfactant content was excluded for this graph since it is much higher than all other values.
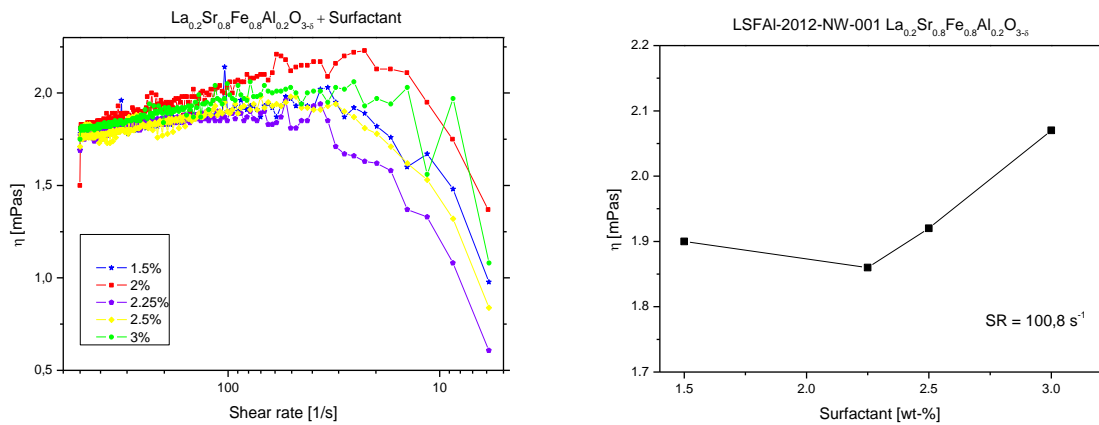
a) Viscosities at shear rates between 500 s^{-1}and 6 s^{-1} b) Viscosities at a fixed shear rate of 100,8 s^{-1}

Figure 5.14: Viscosity values of the different suspensions at 20 ± 0.1 °C

From both graphs in Fig. 5.14 it is proven that the suspension offering 2.25% surfactant content offers the lowest viscosity values and thus the smallest interactions between the particles. For this reason combined with results of the particle size distribution it was chosen for the dip coating process.

5.5 Deposition of functional layers and sintering of asymmetric membranes

Dip coating was done as described in section 4.7. The second dip coating process after pre sintering was done to ensure gas tightness, since contamination of the suspension or the porous support could lead to pin hole formation and thus cause leakage in the resulting membrane. First membranes were doubly dipped and sintered finally at 1175 and 1200 °C for 2 h. For morphology analysis, cross section and surface micrographs were taken with SEM (Fig. 5.15). To generate cross sections the membranes were broken in a controlled manner using pincers.

a) 1175 °C cross section   b) 1175 °C surface

c) 1200 °C cross section   d) 1200 °C surface
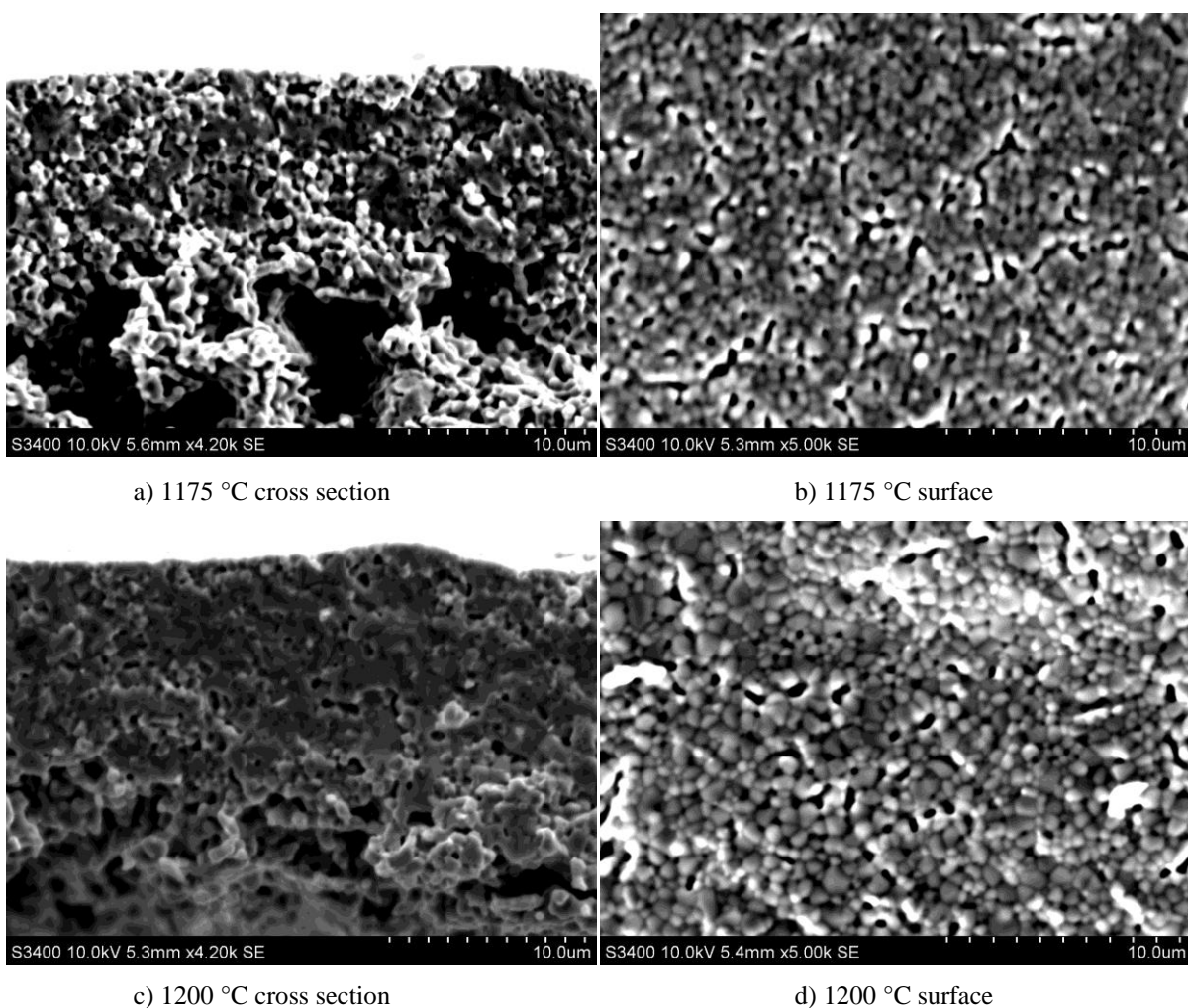
Figure 5.15: SEM micrographs of surface and cross section of asymmetric membranes

All parts of Fig. 5.15 clarify that neither sintering at 1175 °C nor at 1200 °C is sufficient to form a dense layer. An increased density at 1200 °C is evident but still a lot of pores are

apparent. Also the layer is about 10 µm which is quite thin, hence later on membranes were triply dipped to increase layer thickness.

Final parameters for asymmetric membrane production thus were two times 5 s dip coating on the calcined support with a drying step of 10 min. Pre sintering at 1100 °C for 1 h, final dip coating for 5 s on the pre sintered membrane and sintering at 1230 °C for 2 h. Heat treatment programs can be found in section 4.7.

Membranes prepared using these parameters were also characterized by SEM. Sample preparation was done in the same way as described before. Fig. 5.16 shows cross section and surface views of a triply dip coated asymmetric membrane sintered at 1230 °C for 2 h.

a) Cross section   b) Cross section on higher magnification

c) Cross section on lower magnification   d) Surface view, note different magnifications
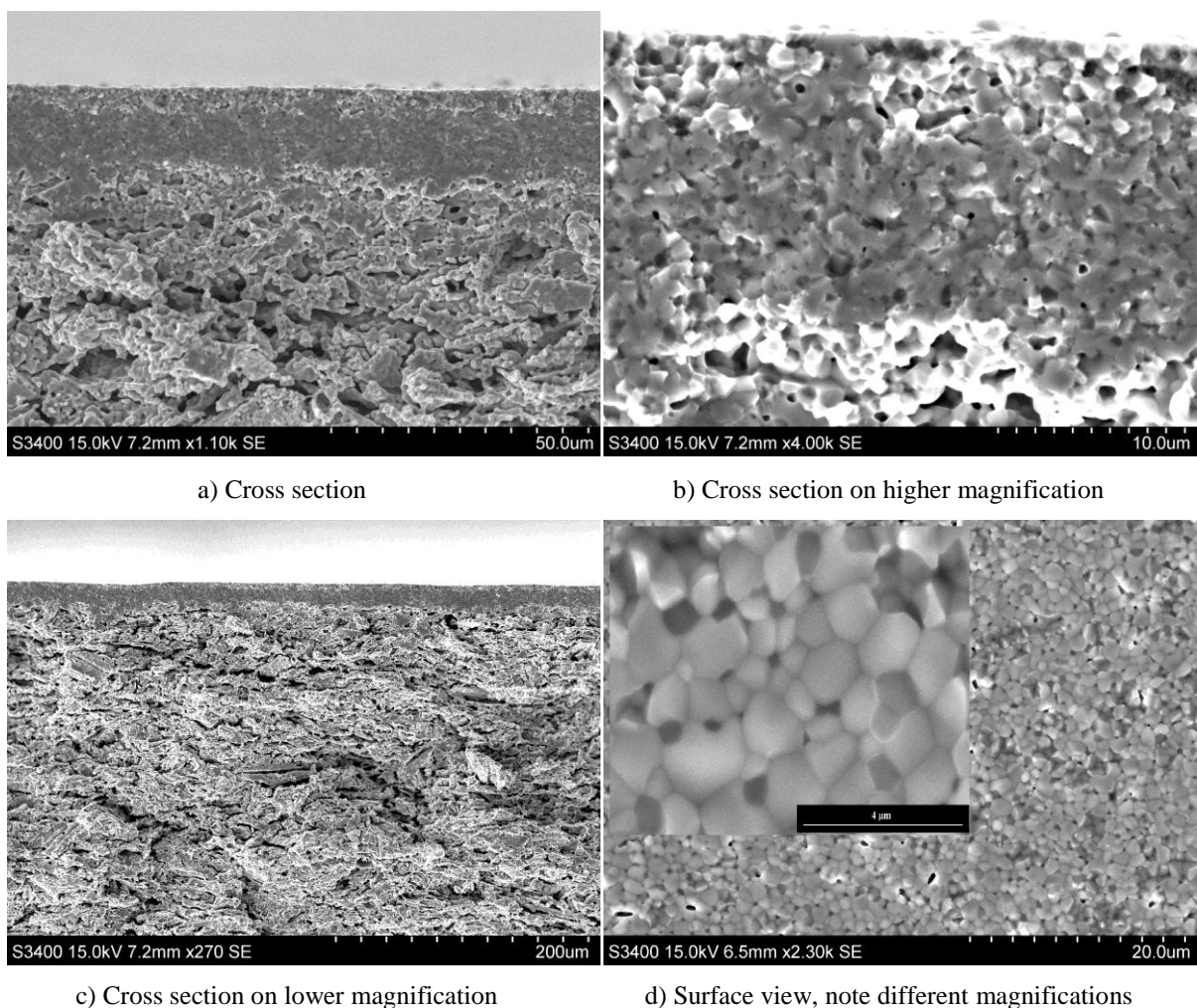
Figure 5.16: SEM micrographs of surface and cross section of an asymmetric membrane manufactured on final parameters

The SEM micrographs showing a dense layer with a thickness of 15-20 µm deposited on a highly porous support. The surface density is also improved compared with samples sintered

at 1175 and 1200 °C. The average grain size is about 1 μm but also a number of sub micron grains are apparent. Furthermore, no secondary phases were detectable using the BSE detector and XRD. XRD pattern is illustrated in Fig. 5.17.
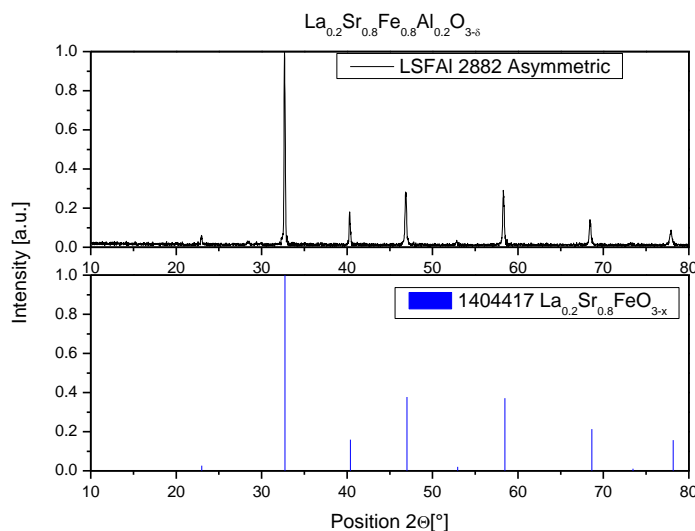
Figure 5.17: XRD pattern of a sintered asymmetric membrane surface

Asymmetric membranes produced by this route resulted in a diameter of approximately 16 mm, a height of approx 2.5 mm and were used for permeation measurements.

5.6 Surface structuring

Three asymmetric membranes were wet chemically etched using parameters of D. S. Lagergren, who worked on surface structuring of a similar composition (LSFTa 2882).[26] Optimal parameters to etch this material were figured out to be 5 min in 6 M HCl and afterwards re etch 2 min in 6 M HCl at room temperature.

Parameters were slightly modified so LSFAl 2882 membranes were etched for 1.5, 4 and 5 min in 6 M HCl. Unfortunately the etching behavior of LSFAl 2882 differs completely from the material described by D. S. Lagergren.[26] Directly after dipping the membranes in the acidic bath a heavy reaction was observed. SEM micrographs illustrated in Fig. 5.18 are showing the result of the etching process.

a) 1.5 min etched surface view   b) 1.5 min etched surface view on higher magnification

c) 4 min etched surface view   d) 5 min etched surface view
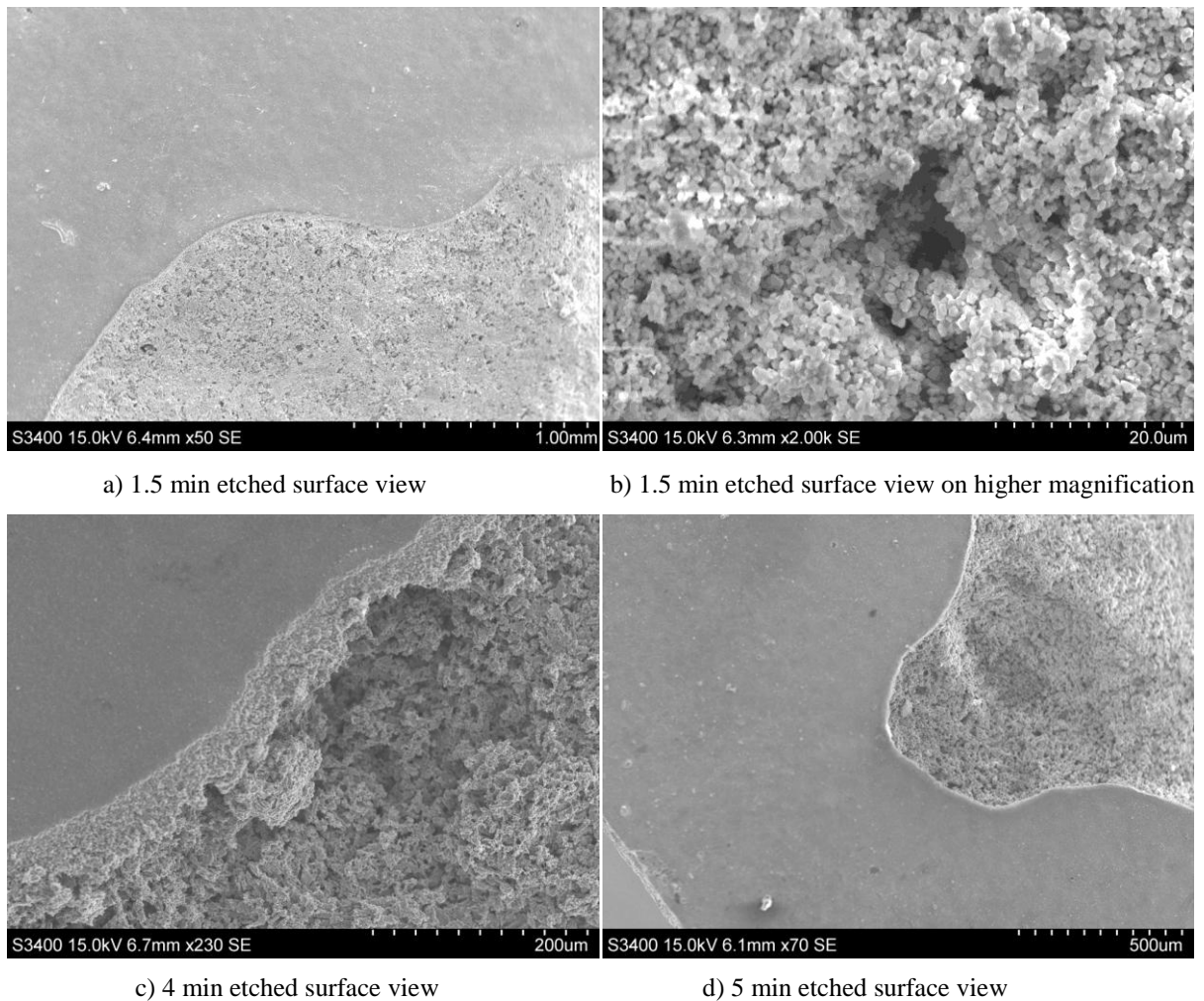
Figure 5.18: SEM micrographs of etched membrane surfaces at different magnifications

It is clearly visible that after 1.5 min of etching already all grain boundaries are dissolved and the layer already exhibits a lot of holes. 4 and 5 min etching in 6 M HCl cause a complete dissolving of the dense layer and thus makes the membranes inoperative.

More experiments on wet chemical etching were not possible due to the limited time of this project.

5.7 Permeation measurements on disk shaped and asymmetric membranes

Permeation measurements were done according to the description in section 4.2.8. Fig. 5.19 shows the oxygen flux as function of the oxygen partial pressure for a 700 µm thick LSFAl 2882 disk. Presented fluxes are average values. Each value was measured five times. In addition the standard deviation of the oxygen flux is included as error bars.
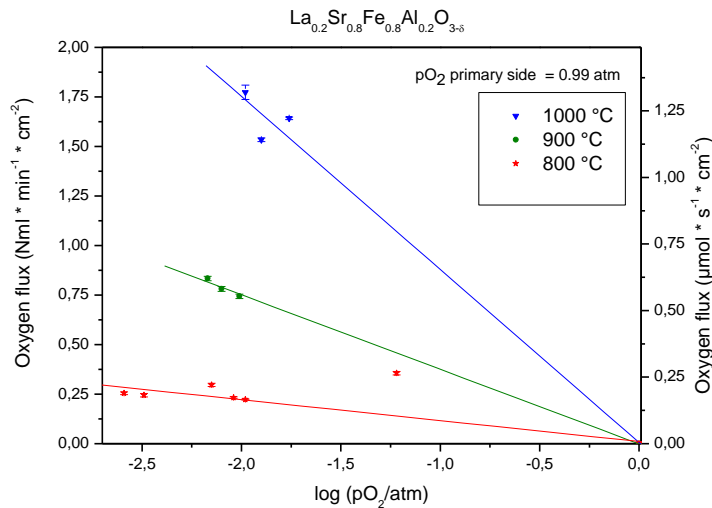
Figure 5.19: Oxygen flux for a 700 µm thick LSFAl 2882 disk. Flow at primary side const. 100 ml/min. Flow at sec. side varies between 6-176 ml/min

All relevant data of the oxygen permeation measurement for the 700 µm thick LSFAl 2882 disk is additionally given in Tab. 5.3.Oxygen flow at the primary side was always kept constant at 100 ml/min.

Table 5.3: Oxygen flux for a 700 µm thick LSFAl 2882 disk

Temp. [°C]	He flow rate on sec. side [ml/min]	log. p_{O2}	Oxygen flux [Nml/min*cm²]	Oxygen flux [µmol/s*cm²]	Standard deviation of oxygen flux
1000	100	-1.76	1.642	1.222	0.006
1000	128	-1.9	1.534	1.142	0.009
1000	176	-1.98	1.773	1.319	0.036
900	80	-2.01	0.744	0.553	0.011
900	104	-2.10	0.781	0.581	0.012
900	128	-2.17	0.834	0.620	0.011
800	6.24	-1.22	0.356	0.265	0.009
800	22.28	-1.98	0.223	0.166	0.002
800	26.74	-2.04	0.233	0.173	0.004
800	44.56	-2.15	0.297	0.221	0.008
800	80	-2.49	0.245	0.182	0.009
800	104	-2.59	0.255	0.189	0.007

Furthermore, the activation energy for oxygen permeation was calculated using the Arrhenius equation. Oxygen flux data was plotted as a common logarithmic Arrhenius plot, keeping the driving force constant at a $\Delta P_{O2} = 0.01$ atm. The natural logarithmic plot can be found in the appendix. The activation energy E_a was calculated to be 123.6 ± 3.7 kJ/mol.
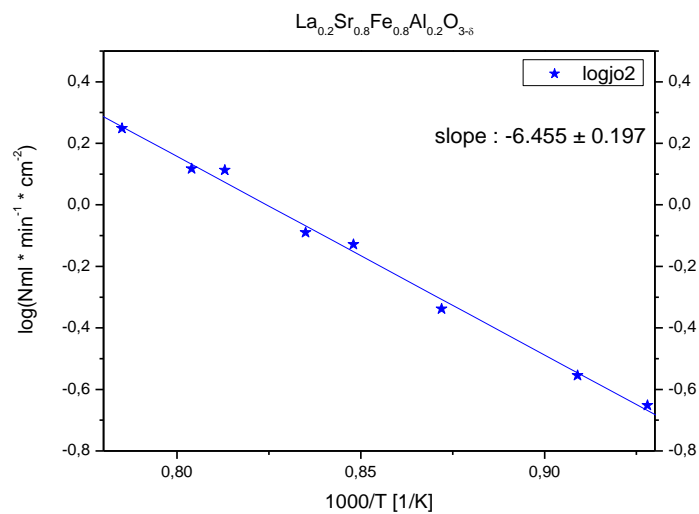
Figure 5.20: Arrhenius plot of a 700 µm thick LSFAl 2882 disk

During the 5% hydrogen exposure of the 700 µm LSFAl 2882 disk, no oxygen was detectable. by the GC, at a H_2/Ar flow rate of 128.68 ml/min on the secondary side. Oxygen flux was thus calculated by determination of residual hydrogen concentration monitored by the GC. Data were taken after 24 and 72 h to monitor the stability of the oxygen flux during hydrogen exposure. Fig. 5.21 shows the oxygen flux values for the 700 µm disk in hydrogen containing atmosphere.
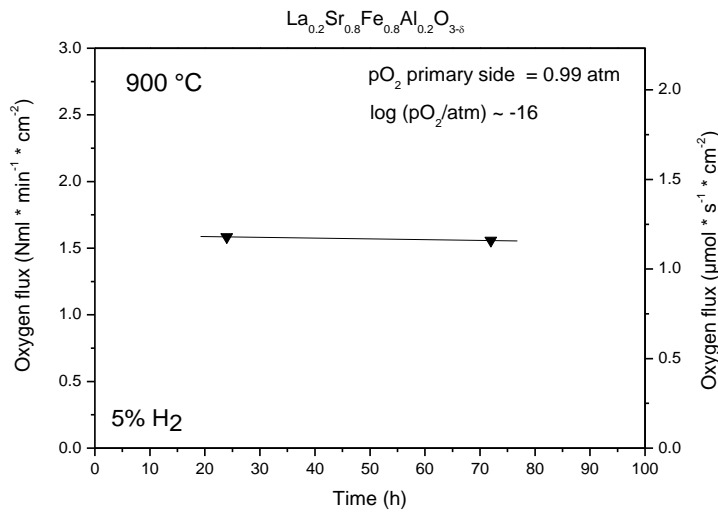
Figure 5.21: Oxygen flux for the 700µm thick LSFAl 2882 disk in 5% H_2 containing atmosphere as a function of time

After 100 h exposing to 5% hydrogen gas the secondary side was exposed to helium again and values were remeasured to check for degradation. Results are plotted in Fig. 5.22.
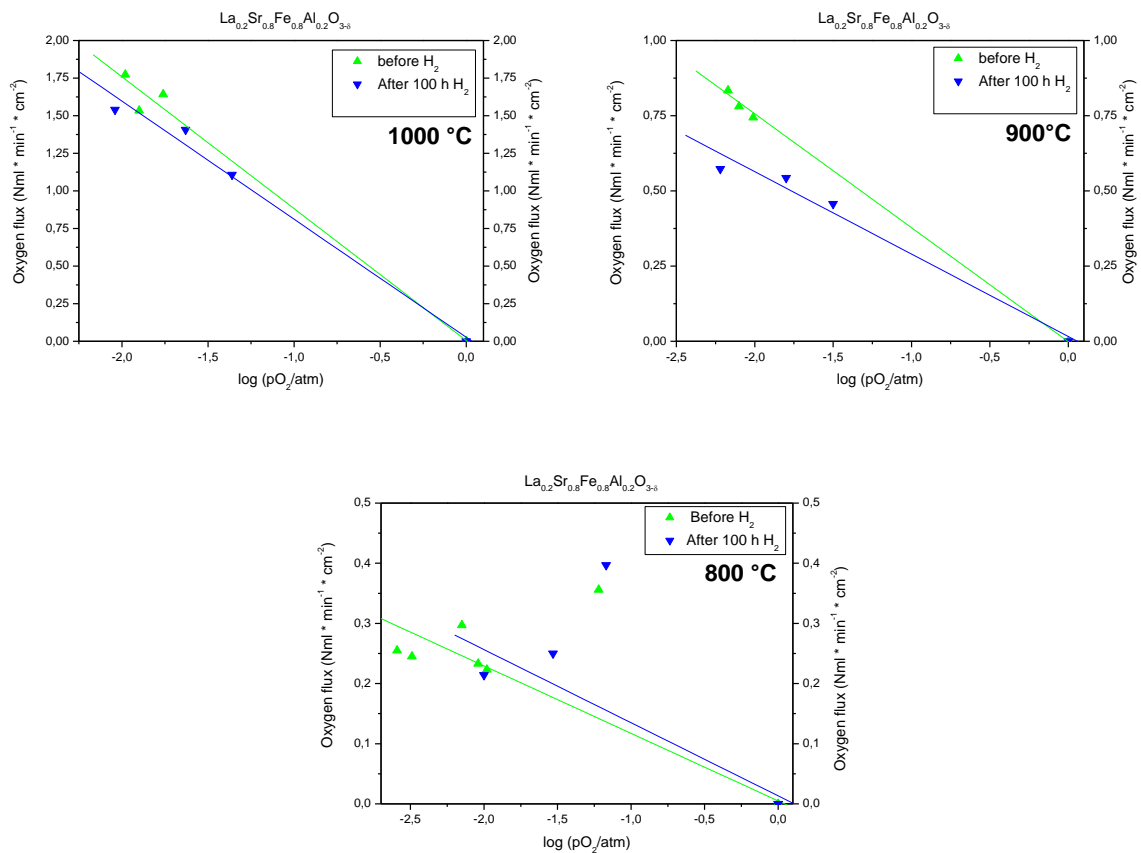
Figure 5.22: Comparison of flux values before and after H_2 expose for a 700 µm thick LSFAl 2882 disk

For 1000 °C and 900 °C a slight decrease of the oxygen flux was detected. The values for 800 °C look randomly distributed what makes it hard to draw conclusions from it.

Oxygen flux as function of the oxygen partial pressure of an asymmetric membrane with a layer thickness of approximately 15-20 µm are illustrated in Fig. 5.23. It reaches values higher than 15 $Nml*min^{-1}*cm^{-2}$ at 1000 °C. Presented fluxes are average values. Each value was measured five times. In addition the standard deviation of the oxygen flux is included as error bars.
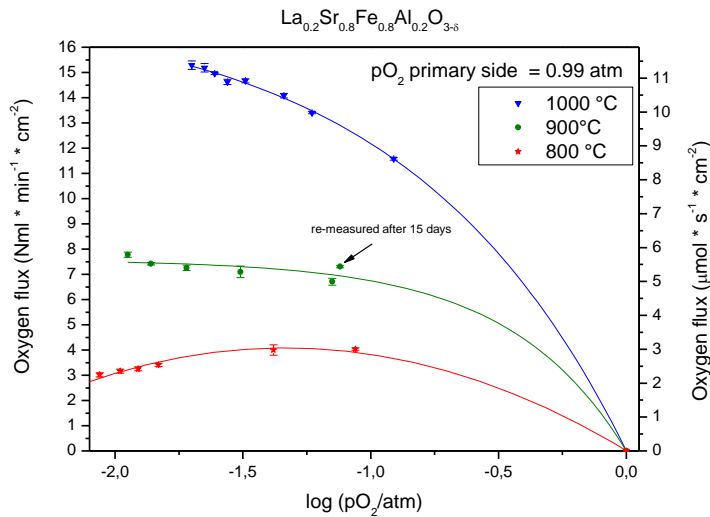
Figure 5.23: Oxygen flux for an approximately15-20 µm thin LSFAl 2882 asymmetric membrane. Flow at primary side const. 100 ml/min. Flow at sec. side varies between 49-800 ml/min

Relevant data of the oxygen permeation measurement for the asymmetric LSFAl 2882 membrane is given in Tab. 5.4. Oxygen flux in the primary side was always kept constant at 100 ml/min

Table 5.4: Oxygen flux for an approximately15-20 µm thin LSFAl 2882 asymmetric membrane

Temp. [°C]	He flow rate on secondary. side [ml/min]	log. p_{O2}	Oxygen flux [Nml/min*cm²]	Oxygen flux [µmol/s*cm²]	Standard deviation of oxygen flux
1000	100	-0.92	11.578	8.617	0.051
1000	240	-1.23	13.405	9.977	0.042
1000	320	-1.34	14.082	10.481	0.087
1000	480	-1.49	14.672	10.920	0.097
1000	560	-1.56	14.626	10.886	0.104
1000	640	-1.61	14.964	11.137	0.049
1000	720	-1.65	15.188	11.304	0.170
1000	800	-1.70	15.293	11.382	0.169
900	100	-1.15	6.708	4.993	0.135
900	240	-1.51	7.098	5.283	0.233
900	400	-1.72	7.255	5.400	0.107
900	560	-1.86	7.421	5.523	0.044
900	720	-1.95	7.776	5.787	0.102
800	49.02	-1.06	4.035	3.003	0.084
800	100	-1.38	4.002	2.979	0.206
800	240	-1.83	3.408	2.536	0.064
800	280	-1.91	3.255	2.423	0.082
800	320	-1.98	3.164	2.355	0.083
800	360	-2.06	3.015	2.244	0.065

After oxygen flux values were measured the membrane was exposed to 5% hydrogen at 900 °C and a flow rate of 128.68 ml/min. After 50 h hydrogen exposure the oxygen flux was measured. Furthermore, the H_2/Ar flow rate was increased to 284.5 ml/min and after conditioning the oxygen flux was measured. Results are given in Fig. 5.24.
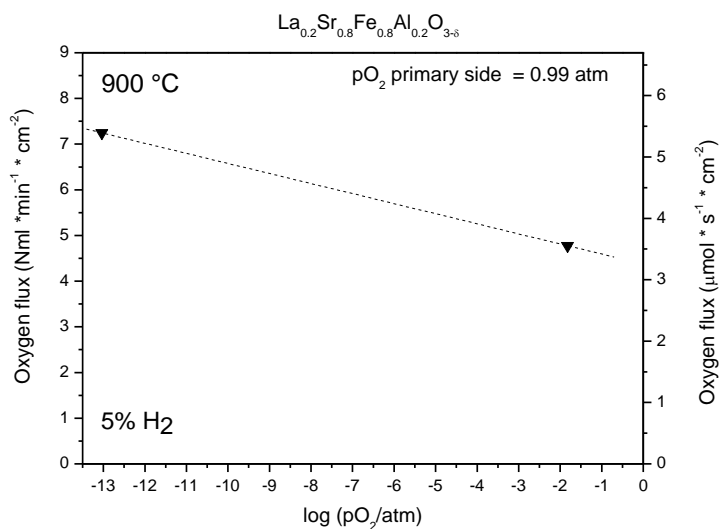
Figure 5.24: Oxygen flux for an approximately15-20 μm thin LSFAl 2882 asymmetric membrane in 5% H_2 containing atmosphere. Flow at primary side const. 100 ml/min. Dashed line included as guide for the eyes

After measurements the gas was changed to 10% hydrogen for 100 h at a flow rate of 128.68 ml/min. During exposure the oxygen flux was measured after 36, 60 and 80 h to monitor the stability of the oxygen flux during hydrogen exposure. Fig 5.25 shows the oxygen flux for the asymmetric membrane during 10% hydrogen exposure as a function of time.
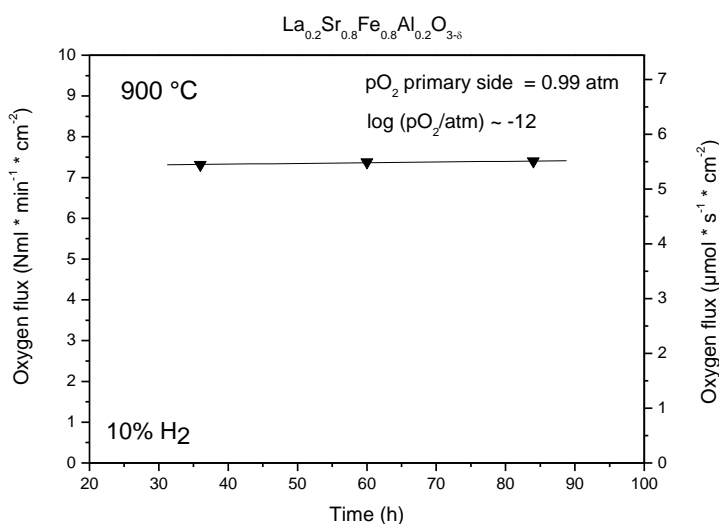
Figure 5.25: Oxygen flux for the asymmetric LSFAl 2882 membrane in 10% H_2 containing atmosphere as a function of time

Once 100 h passed the secondary side was again exposed to helium gas and after conditioning the oxygen flux was remeasured at two different flow rates at 900 °C to control for degradation. The results for a helium flow rate of 240 ml/min are given in Tab. 5.5. The second remeasured value is included in Fig. 5.23.

Table 5.5: Oxygen flux for an approximately15-20 µm thin LSFAl 2882 asymmetric membrane before and after 5 and 10% H_2 exposure

Before Hydrogen exposure					
Temp. [°C]	H_2/Ar flow rate on sec. side [ml/min]	log. p_{O2}	Oxygen flux [Nml/min*cm²]	Oxygen flux [µmol/s*cm²]	Standard deviation of oxygen flux
900	240	-1.51	7.098	5.283	0.233
After Hydrogen exposure					
Temp. [°C]	H_2/Ar flow rate on sec. side [ml/min]	log. p_{O2}	Oxygen flux [Nml/min*cm²]	Oxygen flux [µmol/s*cm²]	Standard deviation of oxygen flux
900	240	-1.52	6.914	5.146	0.116

These values are quite similar, so it can be concluded that there is no significant degradation in oxygen flux.

For the asymmetric membrane the activation energy was calculated at a constant $\Delta(p_{O2}) = 0.01$ atm, to be $E_a = 94.4 \pm 11.3$ kJ/mol. Common logarithmic Arrhenius plot is given in Fig. 5.26. A natural logarithmic plot can be found in the appendix.
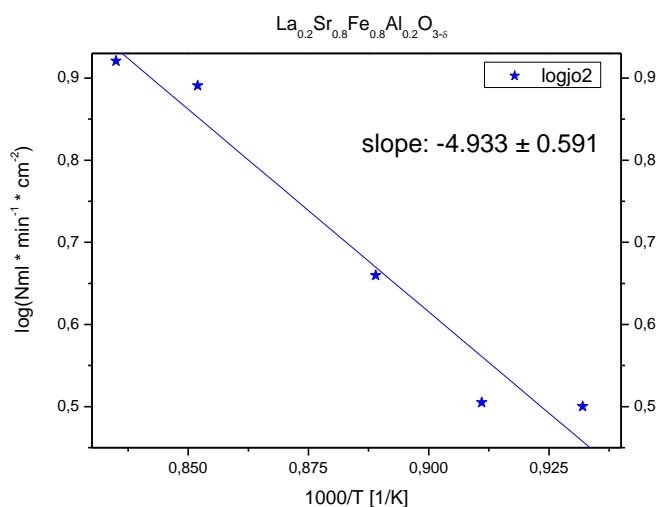
Figure 5.26: Arrhenius plot of an approx. 15-20 µm thin LSFAl 2882 asymmetric membrane

5.8 Degradation studies

To investigate if the material suffer from degradation during operation conditions both LSFAl 2882 disk and asymmetric membrane were analyzed by XRD and SEM/EDS after flux measurements. XRD patterns of the secondary side surface (exposed to He and H_2) of a LSFAl 2882 disk and asymmetric membrane are given in Fig. 5.27. Both, disk and membrane are overall single phase cubic perovskite after approximately 500 h (disk) or 700 h (asymmetric membrane) at high temperatures and different partial pressures including hydrogen exposure for 100 h (disk) or approximately 200 h (asymmetric membrane).

a) disk   b) asymmetric membrane
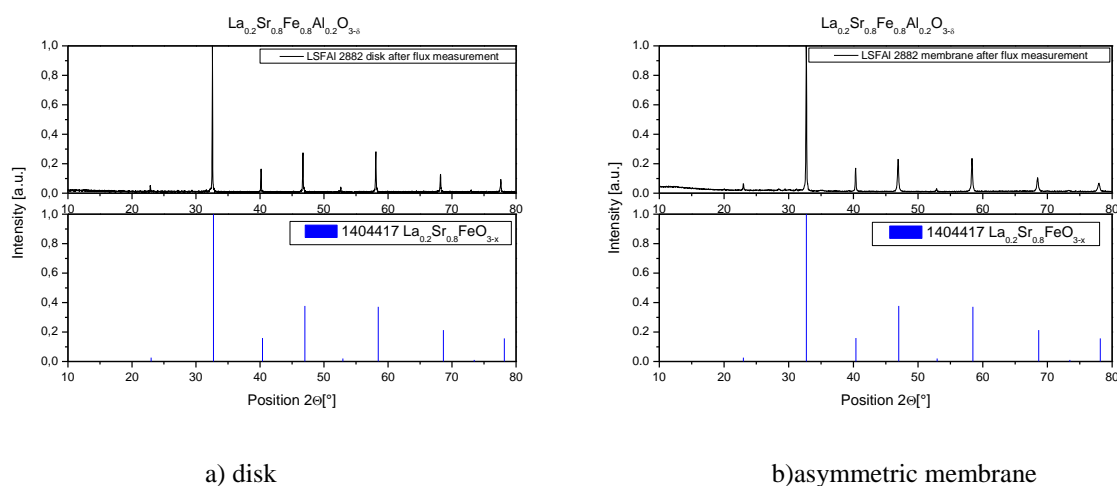
Figure 5.27: XRD patterns of LSFAl 2882 secondary surfaces after flux measurements

Since detection limit of XRD is about 2% and it says nothing about morphological degradation the samples were afterwards examined by SEM/EDS.

Surfaces of both disk shaped and asymmetric membrane offer a different morphology after flux measurements. Fig. 5.28 shows surface micrographs of both kinds of membranes in secondary electron and back scatter electron mode.

a) asymmetric membrane   b) disk shaped membrane
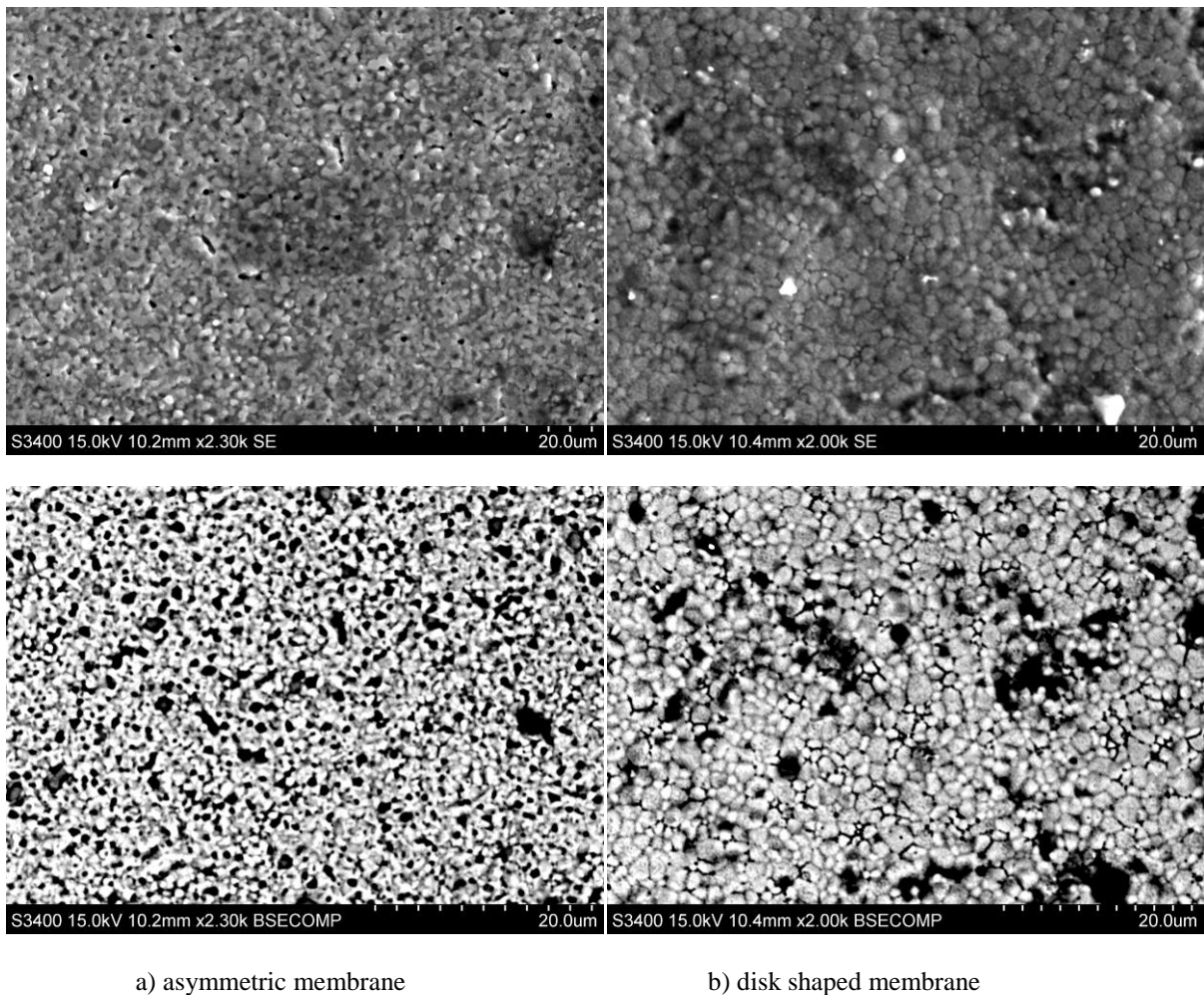
Figure 5.28: SEM micrographs of an asymmetric and disk shaped membrane surface in SE and BSE mode. Taken after exposure to elevated temperatures (800-1000 °C) for 500-700 h including H_2 exposure for 100 h for disk shaped and 200 h for asymmetric membrane

Both membrane show no increase in average grain size, but surface roughness is especially for the asymmetric membrane increased. Larger black areas in the BSE micrographs correspond to contamination of the samples, while smaller areas detect the surface roughness and partly degraded grain boundaries. Micrographs on lower magnification of asymmetric membrane in SE and BSE mode are shown in Fig. 5.29 to clarify an overall phase purity. The dark spots in the BSE mode again correspond to contaminations of the sample. This is clearly visible in the SE micrograph.
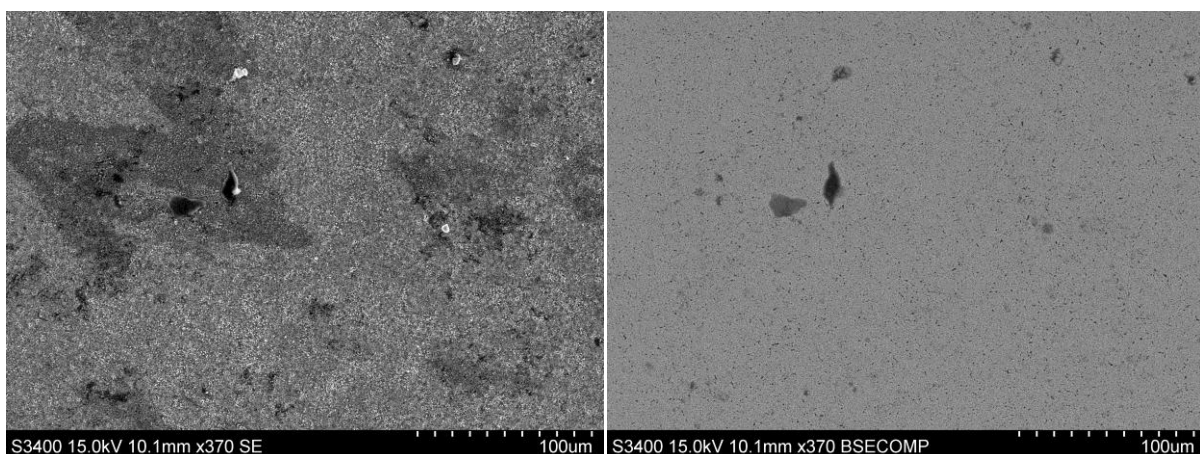
Figure 5.29: SEM micrographs of an asymmetric membrane surface in SE and BSE mode. Taken after exposure to elevated temperatures (800-1000 °C) for 700 h including H_2 exposure for 200 h

Furthermore, a cross section of an asymmetric membrane was investigated to ensure no secondary phases in the bulk of the functional layer. Fig. 5.30 shows SEM micrographs of a cross section in SE and BSE mode.
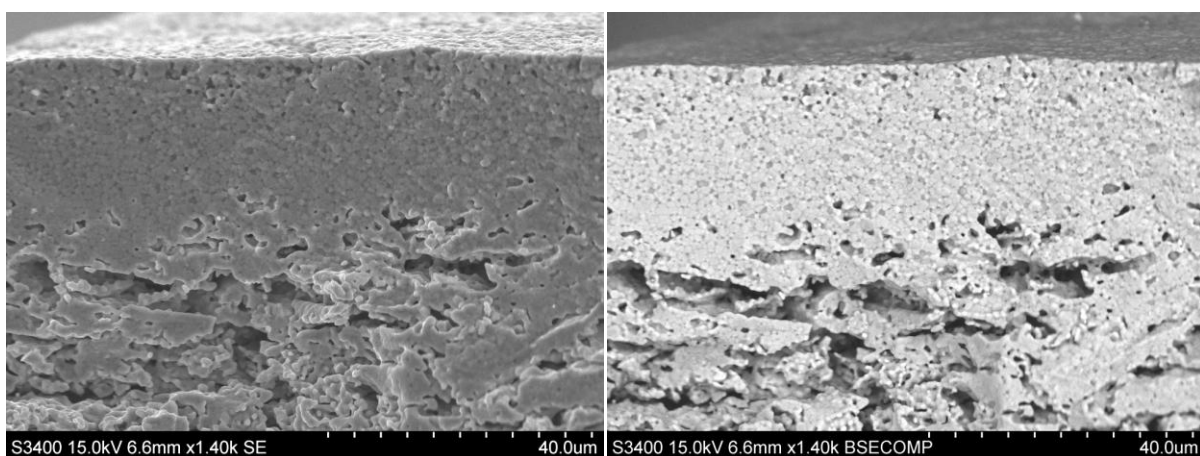
Figure 5.30: SEM micrographs in SE and BSE mode of a cross section of an asymmetric membrane. Taken after exposure to elevated temperatures (800-1000 °C) 700 h including H_2 exposure for 200 h

The BSE micrograph shows a single phase membrane. Furthermore, EDS spectra were taken from two random points of the functional layer. EDS data is given in atomic-% in the following tables. Corresponding spectra can be found in the appendix.

Table 5.6: EDS data a) taken from a random point of the functional layer of Fig. 5.27

Element	Atomic-%
O	50.79
Al	4.44
Fe	21.21
Sr	18.23
La	5.32
Total	100

Table 5.7: EDS data b) taken from a random point of the functional layer of Fig. 5.27

Element	Atomic-%
O	54.8
Al	4.05
Fe	18.9
Sr	17.34
La	4.92
Total	100

It can be concluded that the membrane is overall phase pure. The ratio of the elements is almost identical for the EDS data between the two homogeneous points.

6 Discussion

6.1 Powder properties

For fabrication of dense ceramic samples, mono disperse particles with a small average particle size is a requirement. It was clarified in section 3.5 that powder with a smaller average particle size offers a higher surface energy and thus higher driving force for densification.

High densities, close to the theoretical value, are a requirement for gas tightness of the LSFAl 2882 membranes.

Resulting LSFAl 2882 particle size distribution after ball milling (Fig. 5.4) showed that it was possible to partly reduce the particle size to the size of the primary particles, but still a huge amount of agglomerates was apparent. The calculated particle size from BET data is 106.4 nm. This value is slightly higher than particle size Gurauskis et al. reported for LSFTa 2882 (~84 nm).[12] Both LSFAl 2882 and LSFTa 2882 were synthesized by spray pyrolysis. But, Gurauskis et al. reported a powder calcination at 750 °C, while LSFAl 2882 powder used in this project was calcined at 900 °C. The increased calcination temperature could have an effect on the surface area and explain the different BET results.

A further ball milling with a stabilizing surfactant (Dolacol D 1003) reduced the average particle size even more, so that the biggest amount of particles were in the regime of approximately 200 nm according to DLS. This proves that the agglomerates are rather soft, since they were crushed down by ball milling. Both milled powder and stabilized suspension were proven to be sufficient to manufacture dense disk shaped and asymmetric LSFAl 2882 membranes, which are overall phase pure.

6.2 Disk fabrication

The fabrication of dense, disk shaped, LSFAl 2882 membranes was shown to be unproblematic. Green bodies offered densities about 40% of theor. and showed sufficient strength. Since disks were quite thin (700-800 µm) after sintering, a few samples suffered fractures during the heat treatment. A slow cooling rate from 1000 °C to room temperature helped to fabricate fracture free samples. The reason for fracture formation thus was probably a too rapid cooling, since LSFAl 2882 suffers from chemical expansion due to valence changes of iron. This causes changes in unit cell volume and thus stresses in the material caused by a gradient in the chemical expansion.

6.3 Fabrication of asymmetric membranes

Sample preparation was mostly done according to an article of Gurauskis et al., were the preparation of asymmetric LSFTa 2882 was described.[12] Changes were made in the carbon black addition and the surfactant content for the stabilized suspension was slightly different. Instead of 20 wt-% carbon black, as described by Gurauskis et al.[12] 30 wt% were used. This equals ~ 42 vol-% of the powder mixture and was done to increase the porosity of the supports. Due to the addition of ethyl cellulose binding agent, the green bodies offered a sufficient strength for handling.

Resulting supports offered open porosities of about 47% and SEM micrographs in section 5.3 showed a high degree of inter connected porosity. Permeation values were compared to a porous LSFTa 28882 support, prepared by J. Gurauskis using 20 wt-% carbon black as pore former.[37]
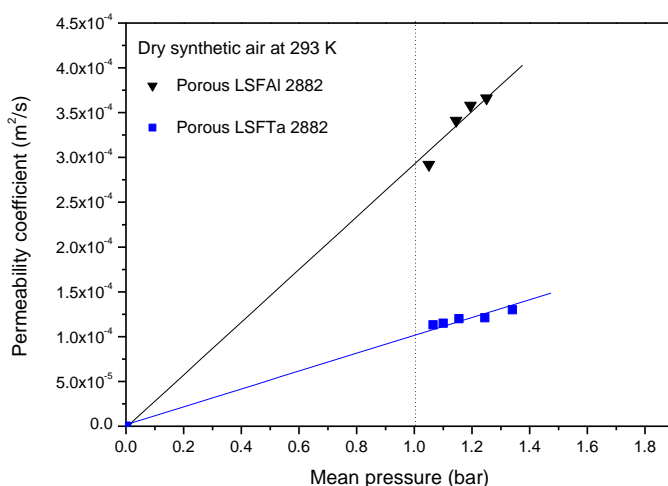
Figure 6.1: Comparison of the permeability of LSFAl 2882 and LSFTa 2882

The increase in gas permeation by a factor of 3 by increasing the pore former content is evident. Furthermore, both supports were sintered at the same temperature.

6.4 Etching behavior

Surface structuring, by means of wet chemical etching, was investigated. The goal was to achieve a higher active surface area and thereby control if the magnitude of the oxygen flux is governed by surface exchange reactions or bulk diffusion. This was done according to a report of D. S. Lagergren, who etched LSFTa 2882 using 6 M HCl. Unfortunately LSFAl 2882 turned out to be less resistant in presence of an acidic environment. Layers partly dissolved already after 1.5 min in 6 M HCl, while LSFTa 2882 layers survived more than 10 min in 6 M HCl.[26] SEM micrographs in section 5.6 showed that it is feasible to generate a higher surface area since LSFAl 2882 surfaces showed a high etching rate. Good results could probably be achieved using more diluted HCl, or a weaker acid and shorter etching time. Also the temperature should be kept on low values $\leq 20\,°C$, since the etching rate is strongly temperature dependent.

Further tests were not feasible and thus it is not possible to give an overall conclusion about the etching behavior of LSFAl 2882.

6.5 Oxygen permeation and stability

LSFAl 2882 disks, offering a thickness of approximately 700 µm, reached oxygen flux values up to 1.77 ml*min^{-1}*cm^{-2} at a $\Delta(p_{O2})$ of 0.01 atm, while asymmetric LSFAl 2882 reaches values up to 15.3 ml*min^{-1}*cm^{-2} at a $\Delta(p_{O2})$ of 0.02 atm. However, the decreasing oxygen flux values, for the asymmetric membrane, by increasing driving force at 800 °C might be some measurement artifact, since values for 900 and 1000 °C increase. The strong increase in oxygen permeation by decreasing the membrane thickness to 15-20 µm clarifies that the magnitude of oxygen flux in disk shaped membranes is governed by bulk diffusion. To achieve more detailed results about the dependence of oxygen flux on the membrane thickness, membranes with different thickness should be measured. If on some region the flux does not increase anymore by decreasing layer thickness, the critical thickness of the material, where the changeover from bulk diffusion to surface exchange reactions occur, would be found.

During hydrogen exposure no oxygen was detectable for the disk shaped membrane. Additionally a cooling trap installed at the exhaust of the permeate (secondary) side clarified water formation, so it can be concluded that the permeated oxygen completely reacts with hydrogen under water formation. By determining the residual hydrogen concentration the oxygen flux was calculated and controlled for stability during the 100 h hydrogen exposure.

For the asymmetric membrane no hydrogen was detectable at an exposure to 5% hydrogen at a flow rate of 128.68 ml/min. In combination with a still existing oxygen net flux of approximately 1.5 Nml/min*cm² it can be concluded that all hydrogen reacted to water. The total oxygen flux was calculated to be 4.8 Nml/min*cm². After exposure to 5% hydrogen the membrane was exposed to 10% hydrogen to induce even more severe reducing conditions. The asymmetric LSFAl 2882 membrane survived 100 h exposure to 10% hydrogen at 900 °C without failure and the oxygen flux was proven to be constant.

The calculated activation energy value for the disk shaped membrane $E_a = 123.6 \pm 3.7$ kJ/mol fits to literature values for similar compositions. Bayraktar et al. reported the activation energy of oxygen permeation through disk shaped $La_{0.5}Sr_{0.5}Fe_{0.8}Ti_{0.2}O_{3-\delta}$, in the temperature region from 875 to 1000 °C, to be 111 kJ/mol.[24] Furthermore, Li et al. reported the activation energy of oxygen permeation through disk shaped $La_{0.2}Sr_{0.8}Fe_{0.8}Co_{0.2}O_{3-\delta}$ to be

123.3 kJ/mol.[34] However asymmetric LSFAl 2882 membrane offered a decreased activation energy $E_a = 94.4 \pm 11.3$ kJ/mol. The activation energies for oxygen flux of disk shaped and asymmetric LSFAl 2882 membranes were compared to activation energies calculated by J. Gurauskis[37]. A comparison is illustrated in Fig. 6.2, in all cases the oxygen partial pressure difference was kept constant at $\Delta(p_{O2}) = 0.01$ atm.
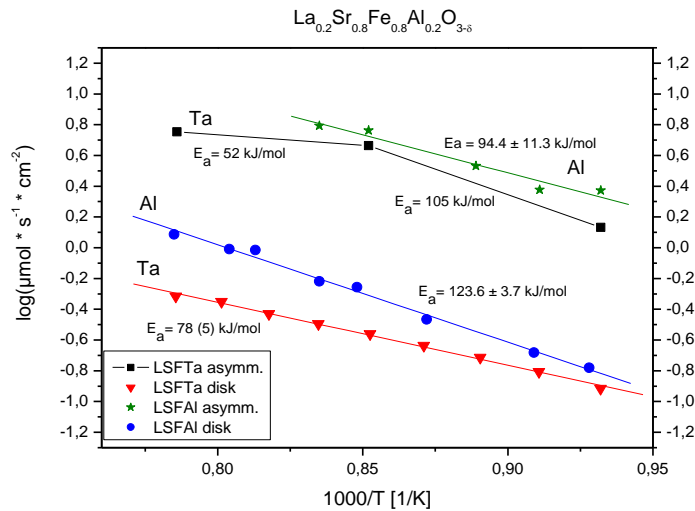

Figure 6.2: Comparison of the activation energies for oxygen flux of LSFAl 2882 and LSFTa 2882

The activation energy for oxygen flux of disk shaped LSFAl 2882 membranes differs strongly from data calculated from J. Gurauskis[37] for disk shaped LSFTa 2882, while the activation energy of asymmetric membranes is quite comparable in temperature regions from 800 to 900 °C. At higher temperatures the asymmetric LSFTa 2882 membrane showed a reduced activation energy, if this is also valid for LSFAl 2882 cannot be concluded since the driving force of $\Delta(p_{O2}) = 0.01$ atm could not be reached with the measurement set up. However the similar activation energy values could indicate that the oxygen transport in both membranes is governed by surface exchange, since Gurauskis et al. reported a oxygen flux increase of almost factor 2 by increasing the active membrane area on the secondary side.[13]

Gurauskis et al. reported oxygen flux values for asymmetric tantalum doped LSF(LSFTa 2882), offering similar membrane thickness, to reach approximately 5 Nml*min^{-1}*cm^{-2} at a $\Delta(p_{O2})$ of about 0.018 atm. Against that the flux value of LSFAl 2882 is 3 times higher.[13] This is an encouraging result especially taking into account that Lohne et al. reported LSFAl

2882 to offer similar stabilities as LSFTa 2882.[11] A comparison of the oxygen flux of LSFAl 2882 and LSFTa 2882[13] at 1000 °C is shown in Fig. 6.3.
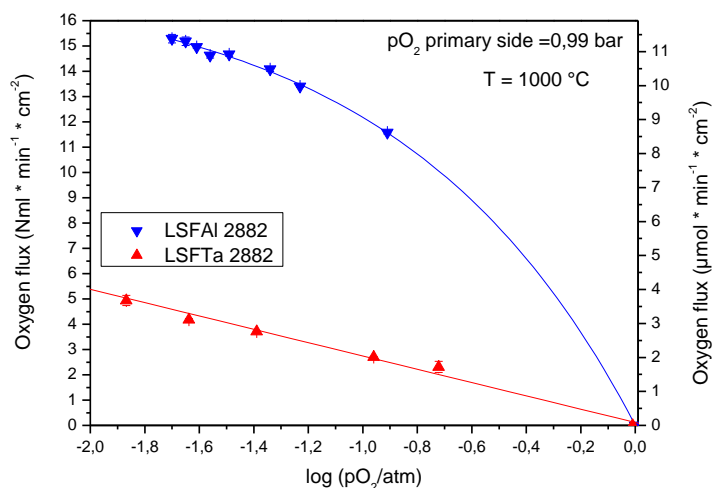

Figure 6.3: Comparison of oxygen flux values of LSFAl 2882 and LSFTa 2882[13] at 1000 °C

As described before, asymmetric membranes, reported by Gurauskis et al. showed a tremendous increase in oxygen flux by increasing the surface area on the permeate side. Thus the magnitude of flux is probably governed by surface exchange kinetics.[13] If the magnitude of oxygen flux for asymmetric LSFAl 2882 membranes is governed by surface exchange kinetics as well, this increase in oxygen flux should also be feasible with surface structured LSFAl 2882 membranes. Since surface exchange rates are dependent on the surface area.

The primary membrane side of asymmetric LSFAl 2882 membranes exhibits, due to geometrical reasons of the interface between porous support and functional layer, already a high surface area.[13]

It cannot be concluded yet which mechanism is responsible for the pronounced flux increase of asymmetric LSFAl 2882 against LSFTa 2882 reported by Gurauskis et al.[13] If in both systems the magnitude of oxygen flux is solely controlled by surface exchange it is dependent on k_{chem} and Δc_O as clarified in section 3.4. Since measurements carried out using the same parameters, the only difference should be the material constant for oxygen exchange k_{chem}, if the magnitude of flux is governed by surface exchange.

It seems to be obvious, that the incorporation of Ta^{5+} on a Fe^{3+} site annihilates oxygen vacancies for charge compensation, while the incorporation of Al^{3+} on a Fe^{3+} site should not have any effect on the oxygen vacancy concentration.

But without the determination of k_{chem} for both systems it cannot be concluded if this is the rate determining step which leads to the strong oxygen flux increase.

A further fact for the high stability of LSFAl 2882 membranes is that it survived 500-700 h at high temperature, different partial pressure and 200 h exposed to 5 and 10% hydrogen containing atmosphere without any failure or significant decrease in oxygen flux values.

Disk shaped membranes showed slightly decrease in oxygen flux at 900 °C, but it cannot be excluded that this phenomena might be a measurement artifact. Especially the oxygen flux values for the disk shaped membrane at 800 °C look completely randomly distributed, what makes it impossible to draw conclusions if the detected decrease in oxygen flux is caused by material degradation.

XRD and SEM/EDS analysis on the permeate (secondary) side of both disk shaped and asymmetric membrane, and SEM/EDS analysis on the cross section of asymmetric membrane resulted in no evidence for secondary phases and clarified overall single phase material after flux measurements.

SEM micrographs in section 5.8 showed the functional layer is still intact. For more detailed considerations if kinetic demixing appears in the grains, EDS mapping on higher resolution or microprobe analysis has to be carried out. Lein et al. investigated the demixing behavior of similar materials and figured out that the mobility of Fe differs from the mobility of La/Sr.[33] It cannot be excluded here that LSFAl 2882 suffer from demixing phenomena on grain size level.

Flux measurements show an effect on the secondary side morphology. SEM images comparing the structure of an asymmetric membrane surface before and after flux measurements are shown in Fig. 6.4.

a) Before flux measurements   b) After flux measurement

c) Before flux measurement (higher magnification)   d) After flux measurement (higher magnification)
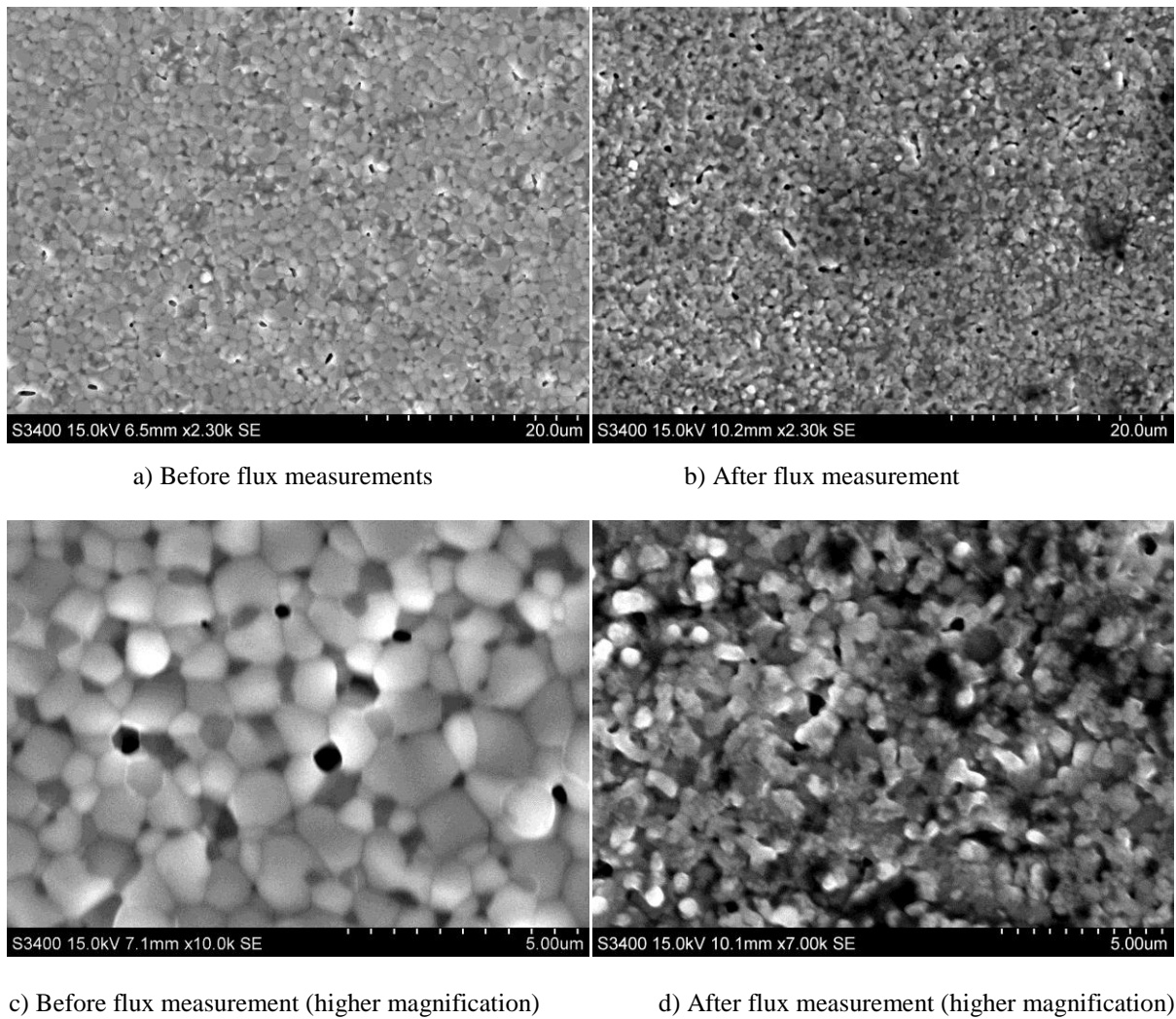
Figure 6.4: SEM micrographs of an asymmetric membrane surface before and after flux measurements

The increased surface roughness is clearly visible. Grain boundaries of the top layer seem to be thermally etched after flux measurements. The same is valid for the secondary side surface of disk shaped membrane. SEM micrographs in section 5.2 show a smooth surface with sharp grain boundaries. Fig. 6.5 shows the secondary side surface of a disk shaped membrane after flux measurements in comparison with a disk shaped membrane before flux measurements. Also here, no grain growth but thermal etched grain boundaries are clearly visible.

S3400 15.0kV 6.5mm x8.50k SE   5.00um | S3400 15.0kV 5.1mm x4.20k SE   10.0um
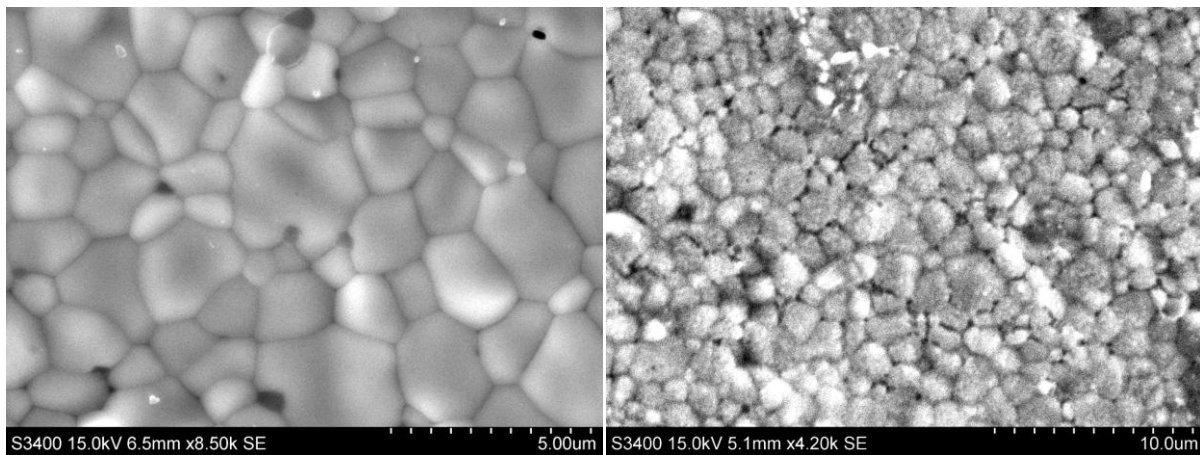
a) Before flux measurements   b) After flux measurements

(note different magnifications)

Figure 6.5: SEM micrograph of the secondary side surface of a disk shaped membrane before and after flux measurements

Combining the flux data and the degradation studies it can be concluded that LSFAl 2882 is a stable composition. Lohne et al. reported Al to improve the stability of LSF with respect to reduction and formation of a brownmillerite phase.[11] Results in this study come to the same result since no secondary phases were formed during the severe conditions of oxygen flux measurements. These results are promising, taking into account that LSFAl 2882 offers oxygen flux values approximately three times higher than LSFTa 2882 reported by Gurauskis et al.[13]

7 Conclusions

- Provided spray pyrolized and calcined powder consisted of softly agglomerated particles. They were partly crushed down by ball milling and almost completely crushed to the primary particle size in presence of the surfactant DOLACOL D 1003
  Hence this method is convenient to prepare dense functional ceramics and layers

- Disked shaped membranes were successfully produced by simple dye pressing and sintering of ball milled powder
  Optimal sintering parameters were 1230 °C for 2 h in air
  Disks reached reproducible 96% of the theoretical density value of LSFAl 2882

- Porous supports produced in this study offered open porosity values of almost 50% and high oxygen permeation at room temperature. This ensures easy gas transport to the active layer of an asymmetric membrane

- Dip coating using a stabilized LSFAl 2882 suspension leads to dense and intact functional layers with a controlled thickness of 15-20 μm
  Optimal sintering parameters for asymmetric membranes were also 1230 °C for 2 h in air

- All membranes produced in this project were single phase, which is an important matter for the material properties

- Surface structuring is associated with challenges and needs further investigations

- Oxygen flux measurements showed a high oxygen permeation up to
  15.3 Nml*min^{-1}*cm^{-2} at $\Delta(p_{O2}) \sim 0.02$atm and 1000 °C for asymmetric membranes

- Neither secondary phase formation (secondary side) nor mechanical failure occurred during oxygen flux measurements This fits well to results achieved by Lohne et al.[13]

8 Recommendations / Further work

Due to encouraging results in oxygen permeation of asymmetric LSFAl 2882 membranes, it is recommended to further analyze the etching behavior and thus produce LSFAl 2882 membranes with structured surface. Alternatively membranes surface could be structured by abrasion or adding a porous layer on top of the dense functional one as described by Gurauskis et al.[12,13] Comparing then oxygen flux values of structured membranes with those achieved in this study could give further conclusions if the magnitude of flux is governed by surface exchange kinetics.

Furthermore membrane thickness could be varied to get hints about the critical thickness, since, if the magnitude of oxygen flux is surface controlled it is independent on membrane thickness, while in the bulk diffusion regime it is dependent on the membrane thickness.

Also the surface exchange coefficient k_{chem} should be determined to draw further conclusions why LSFAl 2882 shows approximately 3 times higher oxygen flux values than LSFTa 2882.

The long term stability under severe conditions might also be examined combined with detailed EDS profiles for demixing on grain size level.

9 Acknowledgements

10 References

[1]   H. J.M. Bouwmeester, *Dense ceramic membranes for methane conversation, Catalysis Today* **2003,** *82, 141-150.*

[2]   H. J.M. Bouwmeester, H. Kruidhof, A.J. Burggraaf, *Importance of the surface exchange kinetics as rate limiting step in oxygen permeation through mixed-conducting oxides, Solid State Ionics* **1994,** *72, 185-194.*

[3]   I. Kaus, K. Wiik, K. Kleveland, B. Krogh, S. Aasland, *Oxygen transport properties in $La_{1-x}Sr_xFe_{1-y}M_yO_{3-\delta}$ (M=Cr, Ti), 0.2<x<0.8, 0.2<y_{Ti}<0.5, 0.1<y_{Cr}<0.3, Solid State Ionics,* **2007,** *178, 817-826.*

[4]   H. Luo, Y. Wei, H. Jiang, W. Yuan, Y.Lv, J. Caro, H. Wang, *Performance of a ceramic membrane reactor with high oxygen flux Ta-containing perovskite for the partial oxidation of methane to syngas, Journal of Membrane Science,* **2010,** *350, 154-160.*

[5]   J. B. Goodenough, *Electronic and ionic transport properties and other aspects of perovskites, Reports on Progress in Physics,* **2004,** *67, 1915-1993.*

[6]   I. Wærnhus, *Defect chemistry, conductivity and mass transport of $La_{1-x}Sr_xFeO_{3-\delta}$ (x=0 and 0,1), Doctoral Thesis at NTNU,* **2003,** *12-35.*

[7]   G. Watterud, *Determination of oxygen transport coefficients in perovskites and perovskite related materials with mixed conductivity, Doctoral Theses at NTNU,* **2005,** *191, 97-120.*

[8]   V.M. Goldschmidt, T. Barth, G. Lunde, W. Zachariasen, *Geochemische verteilungsgesetze der Elemente, Pt. VII Skrifter, Det Norske videnskabs-akademi*, Oslo, **1926**

[9]   A. Fossdal, M.-A. Einarsrud, T. Grande, *Mechanical properties of LaFeO3 ceramics, Journal of the European Ceramic Society,* **2005,** *25, 927-933.*

[10]   A. Fossdal, M. Menon, I. Wærnhus, K. Wiik, M.-A. Einarsrud, T. Grande, *Crystal Structure and Thermal Expansion of La1-xSrxFeO3-δ Materials, Journal of the American Ceramic Society,* **2004,** *87, [10], 1952-1958.*

[11]   Ø.F. Lohne, J. Gurauskis, T.N. Phung, T. Grande, H.J.M. Bouwmeester, K. Wiik, *Effect of B-site substitution on the stability of $La_{0.2}Sr_{0.8}Fe_{0.8}B_{0.2}O_{3-\delta}$,B=Al, Ga,   Cr, Ti, Ta, Nb, Solid State Ionics*, **2012,** *in press, corrected proof.*

[12]   J. Gurauskis, Ø.F. Lohne, H.L. Lein, K. Wiik, *Processing of thin film ceramic membranes for oxygen separation, Journal of the European Ceramic Society,* **2012,** *32* *649-655.*

[13]   J. Gurauskis, Ø.F Lohne,, K Wiik., *La0.2Sr0.8Fe0.8Ta0.2O3-delta based thin film membranes with surface modification for oxygen production. Solid State Ionics,* **2012,** *in press, corrected proof.*

[14]   F.A. Kröger, *The chemistry of imperfect crystals Vol. 2, North-Holland Publishing Company-Amsterdam 1964, Berichte der Bunsengesellschaft für physikalische Chemie,* **1964,** *68, 6, 608.*

[15]   J. Mizusaki, M. Yoshihiro, S. Yamauchi, K. Fueki, *Nonstoichiometry and Defect Structure of the Perovskite-Type Oxides $La_{1-x}Sr_xFeO_{3-\delta}$, Journal of Solid State Chemistry,* **1985,** *58, 257-266.*

[16]   S. E. Dann, D. B. Currie, M. T. Weller, M. F. Thomas, A. D. Al-Rawwas, *The Effect of Oxygen Stoichiometry on Phase Relations and Structure in the System $La_{1-x}Sr_xFeO_{3-\delta}$ ($0 \leq x \leq 1$, $0 \leq \delta \leq 0.5$), Journal of Solid state chemistry,* **1994,** *109, 134-144.*

[17]   S. Nakayama*, LaFeO3 perovskite-type oxide prepared by oxide-mixing, co-precipitation and complex synthesis methods, Journal of Materials Science,* **2001,** *36, 5643-5648.*

[18]   C. Y. Park, T. H. Lee, S. E. Dorris, U. Balachandran, *Hydrogen production from fossil and renewable sources using an oxygen transport membrane, International Journal of Hydrogen Energy,* **2010,** *35, 4103-4110.*

[19]   E. Bartonickova, K. Wiik, K. Maca, H. L. Lein, E. A. Rudberg, *Synthesis and oxygen transport properties of $La_{0.2}Sr_{0.8}Fe_{1-x}Ti_xO_{3-\delta}$ (x=0.2, 0.4) intended for syn-gas production, Journal of the European Ceramic Society,* **2010,** *30, 605-611.*

[20]   J. E. ten Elshof, H. J. M. Bouwmeeskr, H. Verweij, *Oxygen transport through $La_{1-x}Sr_xFeO_{3-\delta}$ membranes II. Permeation in air/CO, CO, gradients, Solid State Ionics,* **1996,** *89, 81-92.*

[21]   H.Salmang, H.Scholze, *Keramik, 7.,vollständig neubearbeitete und erweiterte Auflage, Herausgegeben von R. Telle, ISBN-10 3-546-63273-5, Springer Berling Heidelberg New York,* **2007,** *313-347.*

[22]   M. Matsuka, I. E. Agranovski, R. D. Braddock, *Preparation of asymmetric perovskite-type membranes by a settlement method, Ceramics International,* **2010,** *36, 643-651.*

[23] J. Sunarso, S. Baumann, J.M. Serra, W.A. Meulenberg, S. Liu, Y.S. Lin, J.C. Diniz da Costa, *Mixed ionic–electronic conducting (MIEC) ceramic-based membranes for oxygen separation, Journal of Membrane Science,* **2008,** *320, 13–41.*

[24] D. Bayraktar, S. Diethelm, T. Graule, J. Van herle, P. Holtappels*, Properties of B-site substituted La$_{0.5}$Sr$_{0.5}$FeO$_{3-\delta}$ perovskites for application in oxygen separation membranes, Journal of Electroceramics,* **2009,** *22, 55–60.*

[25] D. S. Lagergren, *Nanostructuring of Oxygen Permeable Membrane Surfaces by Wet Chemical Etching, Specialization Project, Norwegian University of Science and Technology,* **2011.**

[26] E. T. Wefring, *Nanostructuring of oxygen permeable membranes by chemical etching techniques. Diploma thesis, Norwegian University of Science and Technology,* **2011.**

[27] D. A. Slade, Q. Jiang, K. J. Nordheden, S. M. Stagg-Williams*, A comparison of mixed-conducting oxygen-permeable membranes for CO2 reforming, Catalysis Today,* **2009,** *148,290–297.*

[28] R.D Shannon, *Revised Ionic Radii and Systematic Studies of Interatomic Distances in Halides and Chalcogenids, Acta Crystallographica,* **1976,** A 32, 751-767.

[29] C. Tsai, A. G. Dixon, Y. H. Ma, W. R. Moser, M. R. Pascucci, *Dense Perovskite, La$_{1-x}$A*$_{x}$Fe$_{1-y}$Co$_{y}$O$_{3-d}$ (A* = Ba, Sr, Ca), Membrane Synthesis, Applications, and Characterization, Journal of the American Ceramic Society,* **1998,** *81, 6, 1437–1444.*

[30] S. Diethelm, D. Bayraktar, T. Graule, P. Holtappels, J. Van herle, *Improved stability of La0.5Sr0.5FeO3 by Ta-doping for oxygen separation membrane application, Solid State Ionics,* **2009,** *180, 857-860.*

[31] Pearsons's Crystal Data Base, *La$_{0.2}$Sr$_{0.8}$FeO$_{3-\delta}$ entry number 1404417.*

[32] T. N. Phung, *oral communication about theoretical density of LSFAl 2882. PhD student at University Twente, e-mail: t.phungnhuttan@tnw.utwente.nl.*

[33] H. L. Lein, K. Wiik, T. Grande, *Kinetic demixing and decomposition of oxygen permeable membranes, Solid State Ionics,* **2006,** *177, 1587-1590.*

[34] S. Li, W. Jin, P. Huang, N. Xu, J. Shi, Y.S. Lin, Z.C. Michael and E. Payzant, *Comparison of oxygen permeability and stability of perovskite type La$_{0.2}$A$_{0.8}$Co$_{0.2}$Fe$_{0.8}$O$_{3-\delta}$ (A = Sr, Ba, Ca) membranes, Ind. Eng. Chem. Res.,* **1999,** *38, 2963–2972.*

[35] J. Maier, *On the correlation of macroscopic and microscopic rate constants in solid state chemistry, Solid State Ionics,* **1998,** *112, 197–228.*

[36]   F. W. Altena, H. A. M. Knoef, H. Heskamp, D. Bargeman, C. A. Smolders, *Some comments on the applicability of gas permeation methods to characterize porous membranes based on improved experimental accuracy and data handling, Journal of Membrane Science, 12,* **1983,** *313-322.*

[37]   J. Gurauskis, *oral communication about unpublished data concerning issue* [12,13], *Post   Doctoral   Fellow   at   NTNU   Trondheim,   e-mail: jonas.gurauskis@material.ntnu.no.*

[38]   X. Chang, C. Zhang, Z. Wu, W. Jin, N. Xu, *Contribution of the Surface Reactions to the Overall Oxygen Permeation of the Mixed Conducting Membranes, Ind. Eng. Chem. Res.,* **2006,** *45, 2824-2829.*

[39]   H.Salmang, H.Scholze, *Keramik, 7.,vollständig neubearbeitete und erweiterte Auflage, Herausgegeben von R. Telle, ISBN-10 3-546-63273-5, Springer Berling Heidelberg New York,* **2007,** *170-171.*

Appendix Materials

Table of contents

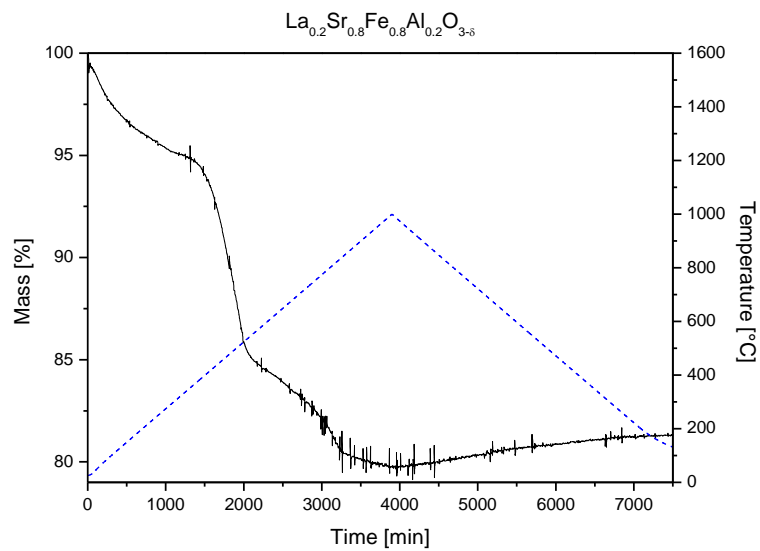# Appendix A: TGA plotted against time and temperature

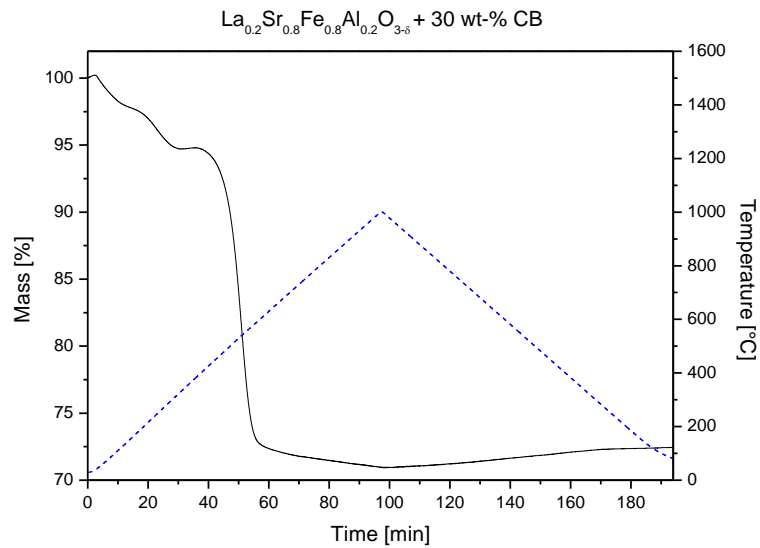Figure A.1: TGA plotted against time of the precursor prior to calcination

Figure A.2: TGA plotted against time of LSFAl 2882 + 30 wt-% carbon black

Appendix B: Calculation for a stabilized LSFAl 2882 suspension

7					
8		Solid content		2,5	g
9					
10		Solid load		2	vol. %
11					
12		Powder density		5,54	g/cm^3
13					
14		Solid volume		=F8/F12	ml
15					
16					
17		Solvent volume		=((100-F10)*F14)/F10	ml
18					
19		Solvent density (EtOH)		0,79	g/cm^3
20					
21		Solvent content		=F17*F19	g
22					
23					
24		Surfactant proportion		2	%
25					
26		Surfactant proportion		=(F8*F24)/100	g
27					
28		Surfactant concentration		10	%
29					
30		Surfactant final amount		=(F26*100)/F28	g
31					

Figure B.1: Excel calculation scheme for a stabilized suspension

Appendix C: Oxygen flux calculation

C	D	E	F	G	H	I	J	K	L	M	N	O
Membrane		Disk		Membrane area	1.05	cm2						
Sweep gas		CH4		Aperture	12.5	%						
He	=H9*8		ml/min									
O2	100		ml/min	Sweep gas	run	counts		%		ml/min		ml/min*cm2
				O2 peak counts	1	6221937		=(0.00000196099*I13)		=D13*K13/100		=M13/H8
					2	6205914		=(0.00000196099*I14)		=D13*K14/100		=M14/H8
					3	6187871		=(0.00000196099*I15)		=D13*K15/100		=M15/H8
					4	6157635		=(0.00000196099*I16)		=D13*K16/100		=M16/H8
					5	6223359		=(0.00000196099*I17)		=D13*K17/100		=M17/H8
							pO2"	=MITTELWERT(K13:K17)		=MITTELWERT(M13:M15)		=MITTELWERT(O13:
							Stan. Dev.	=STABW(K13:K15)		=STABW(M13:M15)		=STABW(O13:O17)
												molMol/s*cm2
							pO₂=10^	=LOG(K19*0.01)				=(0.001429*O19)/3:

Figure C.1: Excel calculation of oxygen flux

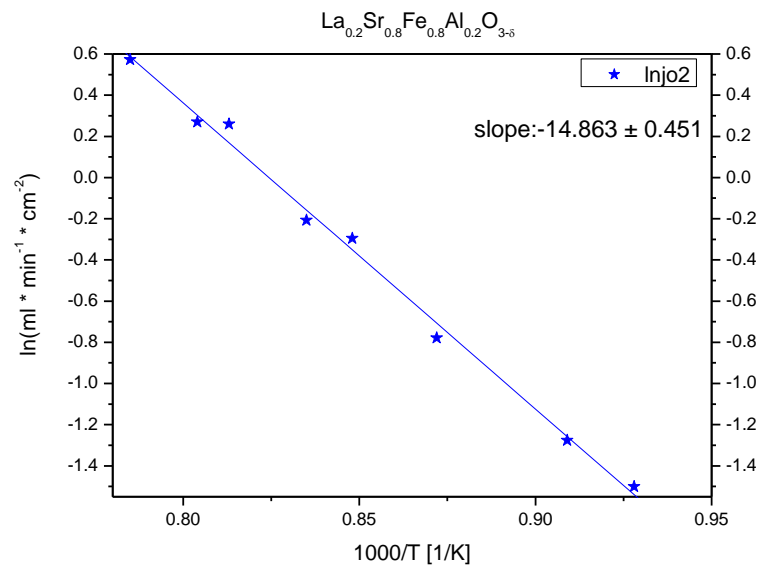## **Appendix D: Activation energy calculations**

Figure D.1: Arrhenius plot of disk shaped membrane

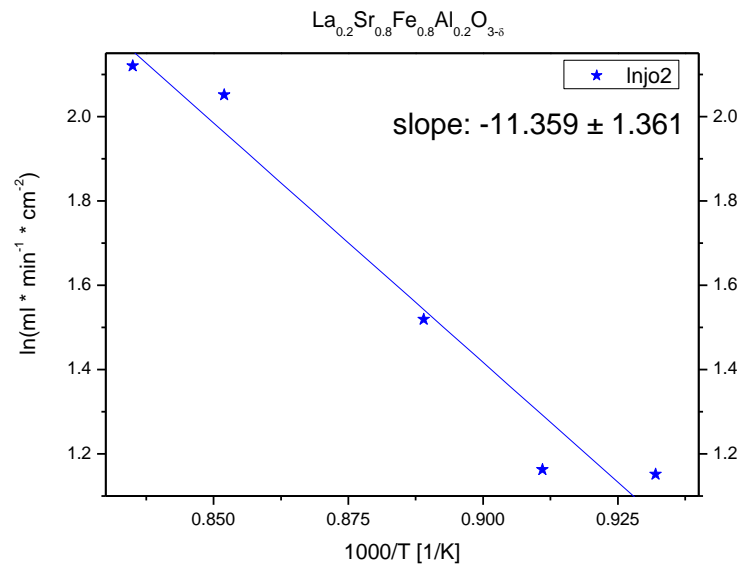$$E_a = |slope| \times R \times 1000 [J/mol]$$
$$E_a = 123.6 \pm 3.7 \text{ kJ/mol } kJ/mol$$

Figure D.2: Arrhenius plot of asymmetric membrane

$$E_a = |slope| \times R \times 1000[J/mol]$$
$$E_a = 94.4 \pm 11.3 \; kJ/mol$$

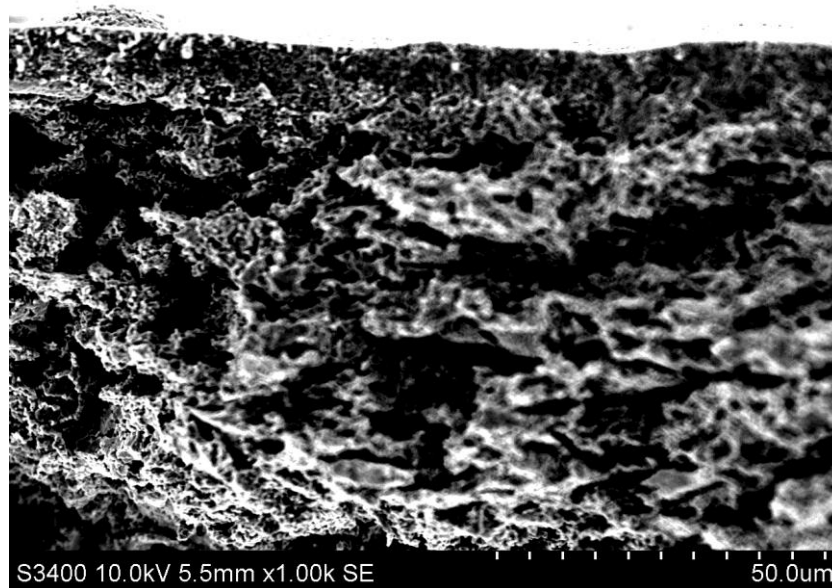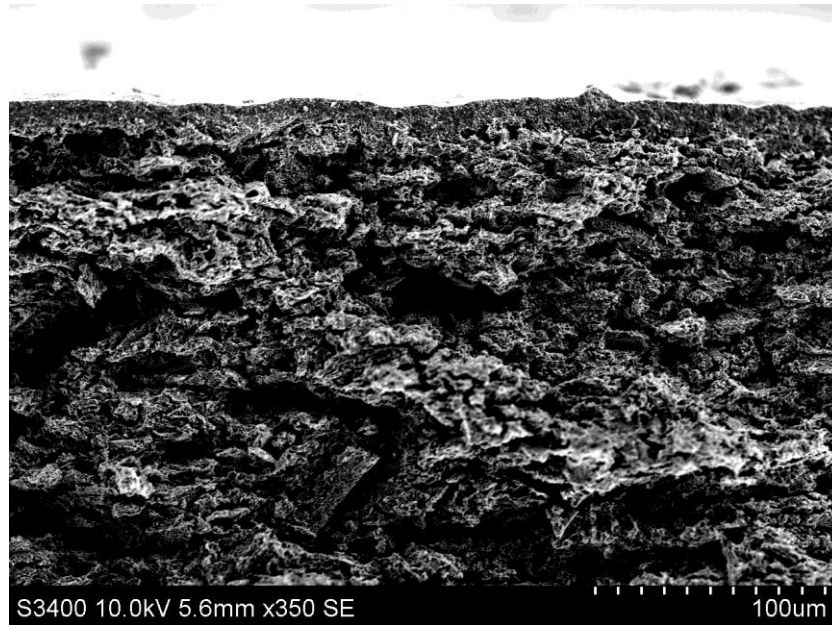# Appendix E: SEM micrographs of asymmetric membrane sintered at 1175 °C

Figure E.1: Cross section micrographs of a asymmetric membrane sintered at 1175 °C

Appendix F: SEM micrographs of asymmetric membrane sintered at 1200 °C
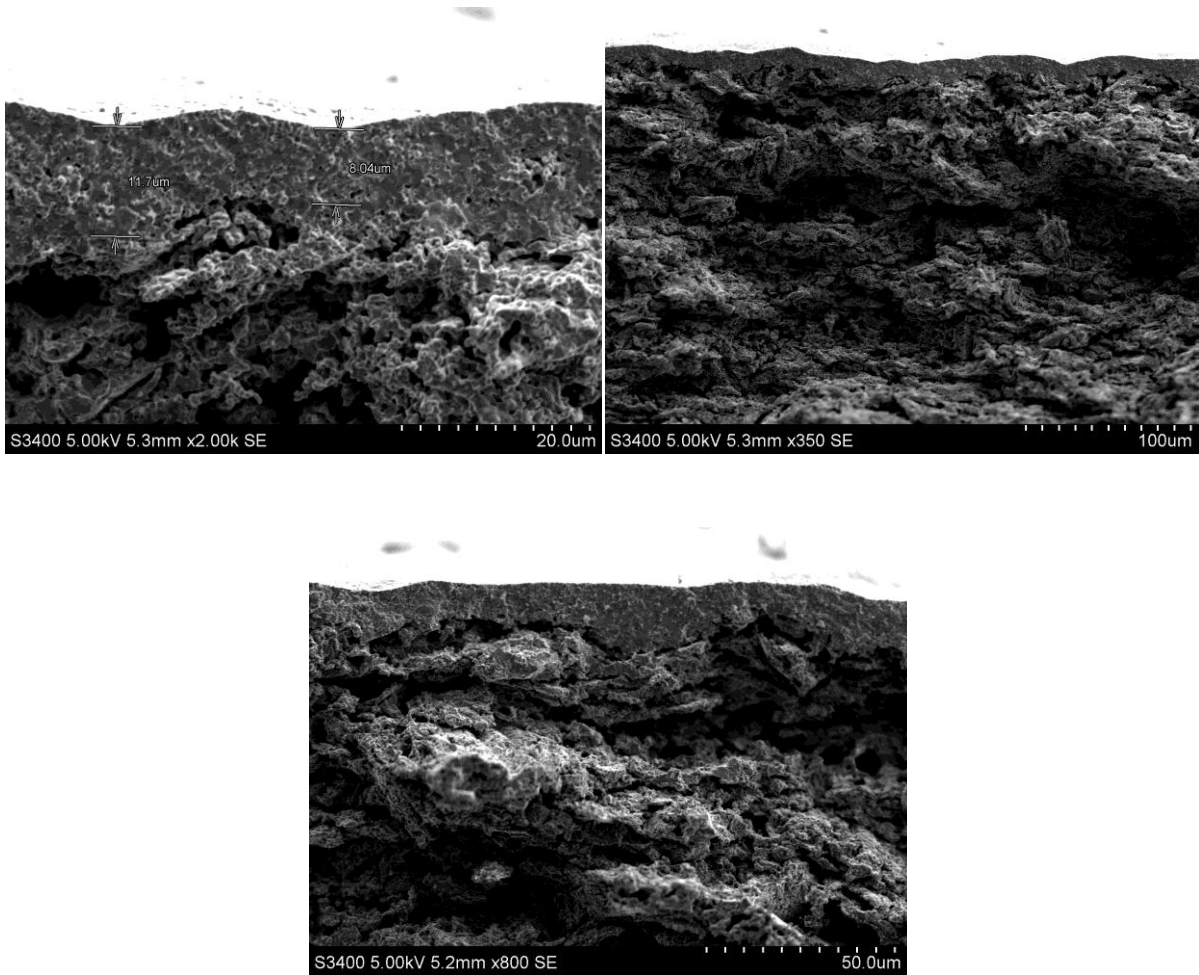
Figure F.1: Cross section micrographs of a asymmetric membrane sintered at 1200 °C

Appendix G: Surface fracture of an asymmetric membrane produced with final parameters
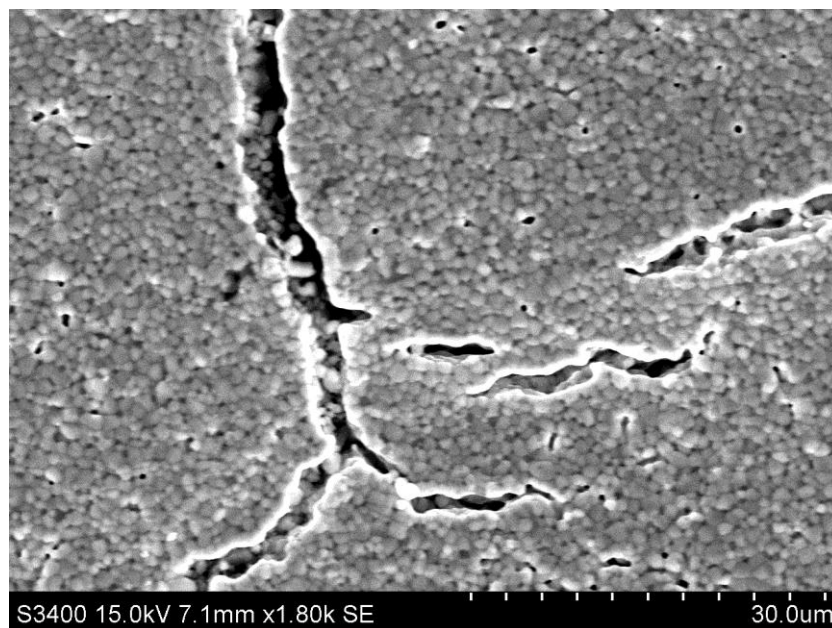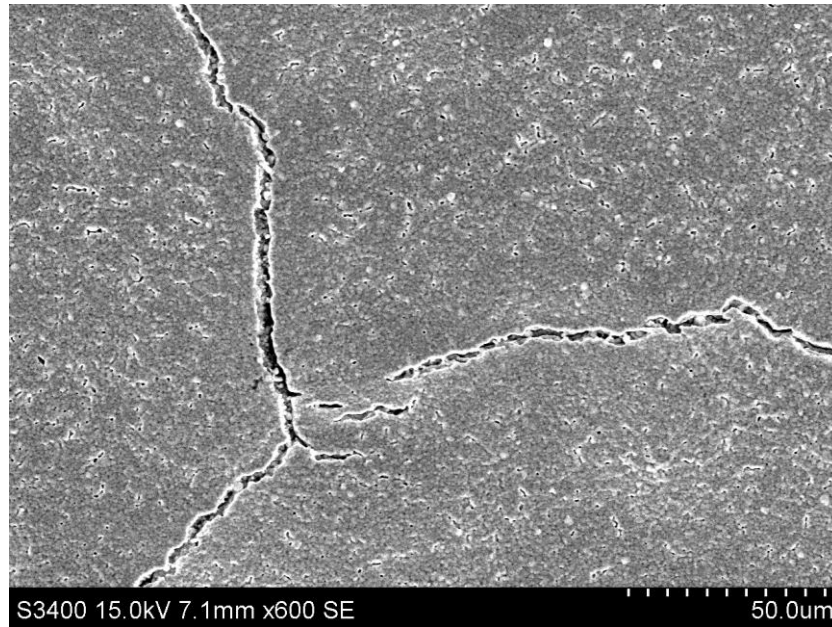

Figure G.1: Surface fractured asymmetric membrane produced on final parameters

Appendix H: EDS spectra

EDS spectra taken from a homogeneous point in the cross section of an asymmetric LSFAl 2882 membrane.
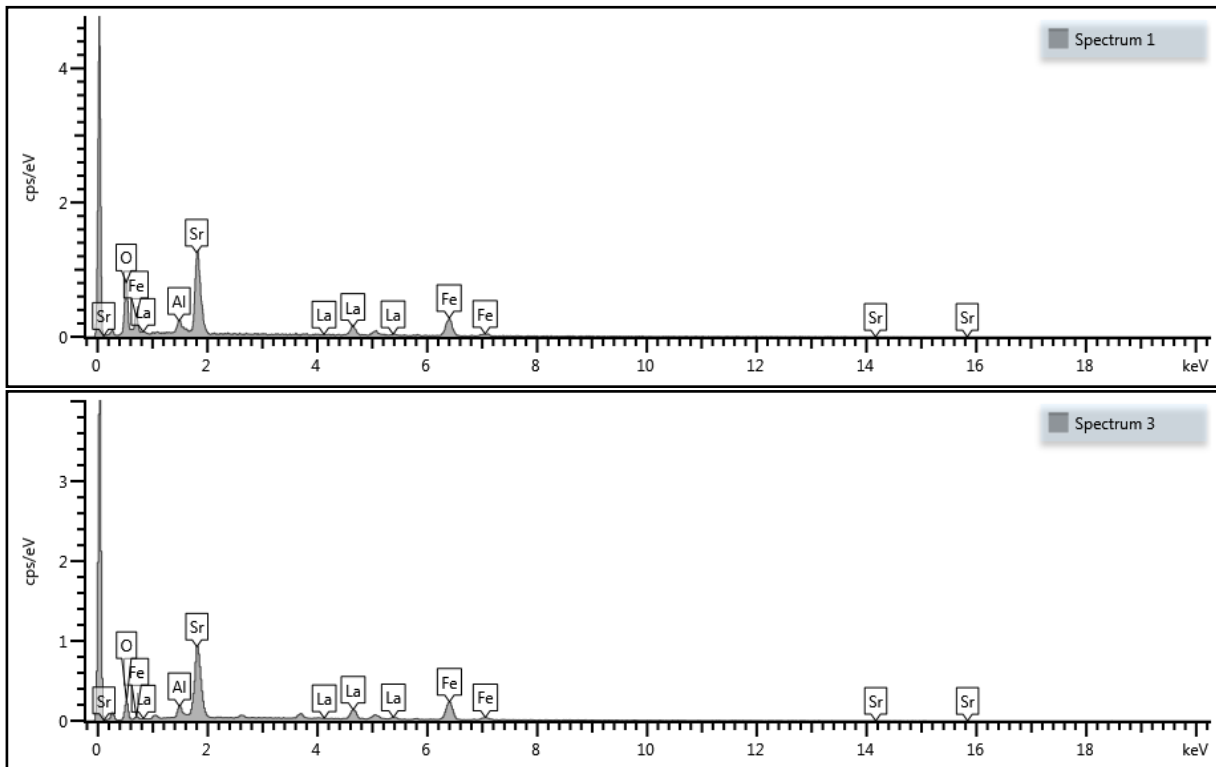

Figure H.1: EDS spectra of two points in a cross section of an asymmetric membrane
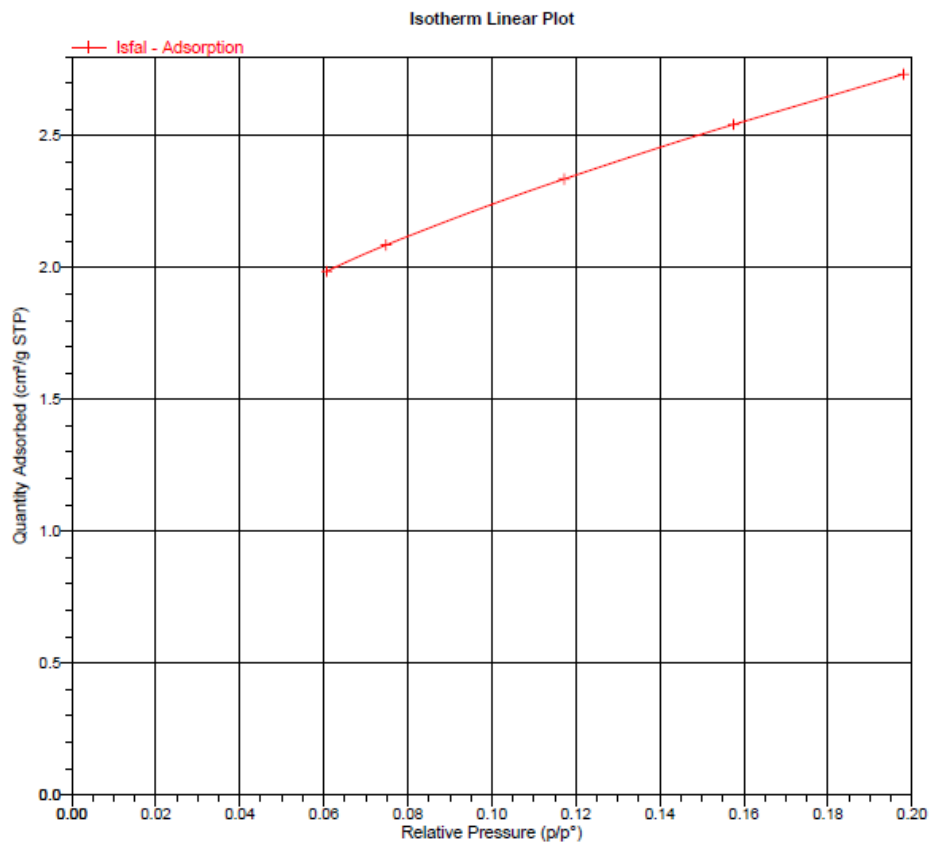
Appendix I: BET Result

Figure I.1: BET Isotherm linear plot

BET Surface Area Report

BET Surface Area: 10.1815 ± 0.0529 m²/g
Slope: 0.420287 ± 0.002202 g/cm³ STP
Y-Intercept: 0.007273 ± 0.000291 g/cm³ STP
C: 58.783986
Qm: 2.3389 cm³/g STP
Correlation Coefficient: 0.9999588
Molecular Cross-Sectional Area: 0.1620 nm²

Relative Pressure (p/p°)	Quantity Adsorbed (cm³/g STP)	1/[Q(p°/p - 1)]
0.060679683	1.9859	0.032530
0.074834116	2.0857	0.038781
0.117210652	2.3360	0.056839
0.157586035	2.5428	0.073566
0.197961418	2.7334	0.090300